Ocean Alkalinity Enhancement in Deep Water Formation Regions Under Low and High Emission Pathways

Tanvi Nagwekar[1] [ID], **Cara Nissen[2]** [ID], **and Judith Hauck[1]** [ID]

[1]Alfred Wegener Institute for Polar and Marine Research, Bremerhaven, Germany, [2]Department of Atmospheric and Oceanic Sciences and Institute of Arctic and Alpine Research, University of Colorado, Boulder, CO, USA

Abstract   Ocean Alkalinity Enhancement (OAE) is an ocean-based Carbon Dioxide Removal (CDR) method to mitigate climate change. Studies to characterize regional differences in OAE efficiencies and biogeochemical effects are still sparse. As subduction regions play a pivotal role for anthropogenic carbon uptake and centennial storage, we here evaluate OAE efficiencies in the subduction regions of the Southern Ocean, the Northwest Atlantic, and the Norwegian-Barents Sea region. Using the ocean biogeochemistry model FESOM2.1-REcoM3, we simulate continuous OAE globally and in the subduction regions under high (SSP3-7.0) and low (SSP1-2.6) emission scenarios. The OAE efficiency calculated by two different metrics is higher (by 8%–30%) for SSP3-7.0 than for SSP1-2.6 due to a lower buffer factor in a high-CO_2 world. All subduction regions show a CDR potential (0.23–0.31; PgC CO_2 uptake per Pg alkaline material) consistent with global OAE for both emission scenarios. Calculating the efficiency as the ratio of excess dissolved inorganic carbon (DIC) to excess alkalinity shows that the Southern Ocean and the Northwest Atlantic are as efficient as the global ocean (0.79–0.85), while the Norwegian-Barents Sea region has a lower efficiency (0.65–0.75). The subduction regions store a fraction of excess carbon below 1 km that is 1.9 times higher than the global ocean. The excess surface alkalinity and thus CO_2 uptake and storage follow the mixed-layer depth seasonality, with the majority of the excess CO_2 flux occurring in summer at shallow mixed layer depths. This study therefore highlights that subduction regions can be efficient for OAE if optimal deployment strategies are developed.

Plain Language Summary   Increasing atmospheric CO_2 concentrations demand urgent reductions in the anthropogenic greenhouse gas emissions to limit the increase in global air temperatures to $\leq 2°C$ relative to preindustrial conditions. To compensate for/counteract the small fraction of unavoidable emissions, it will also be necessary to implement a portfolio of carbon dioxide removal (CDR) methods. In this study, we focus on the ocean-based CDR method Ocean Alkalinity Enhancement (OAE), which enhances oceanic carbon uptake and can thus aid in atmospheric CO_2 reduction. Oceanic subduction regions are key for anthropogenic carbon uptake and its centennial storage. Therefore, we simulate OAE in the deep and bottom water formation regions of the Southern Ocean, Northwest Atlantic and the Norwegian-Barents Sea region to assess their carbon uptake and storage efficiency compared to the global ocean. We find that the subduction regions exhibit equivalent carbon uptake efficiency to the global ocean, and are nearly two times more effective in deep ocean carbon storage with respect to OAE. Seasonal mixed layer depth variability, however, influences the resulting surface alkalinity concentrations and thus CO_2 uptake and DIC accumulation. Therefore, our study emphasizes that the subduction regions can be efficient for OAE when appropriate deployment strategies are developed.

1. Introduction

The Paris Agreement 2015 states that the average global surface temperature increase relative to preindustrial conditions should be limited to well below 2°C and preferably to 1.5°C by the end of the 21st century (UNFCCC, 2015). To reach this goal, the future emission pathways outlined by the Intergovernmental Panel on Climate Change (IPCC) emphasize the crucial role of emissions reductions. However, to attain a trajectory of net negative CO_2 emissions during the second half of the 21st century, deployment of Carbon Dioxide Removal (CDR) approaches are likely unavoidable (Riahi et al., 2022). Consequently, various CDR methods are actively assessed (Gattuso et al., 2021). Studies focusing on land-based CDR approaches highlight conflicts around land use, carbon storage durability, and risk of ecosystem disruption (Fuss et al., 2018). The documented potential impacts on marine ecosystem due to application of certain ocean-based CDR method are not profound and are mostly region specific (Hernández-Hernández et al., 2018). Hence, there is a growing interest to investigate

various marine CDR methods to increase the oceanic carbon uptake and assess the possibility of any side effects it can have on the ecosystem.

Historically, the ocean has played a pivotal role in regulating atmospheric CO_2 concentration by taking up almost a third of anthropogenic CO_2 emitted since the preindustrial times (Friedlingstein et al., 2022). The subduction regions in the ocean play a prominent role by transporting the carbon taken up at the air-sea interface to the deep ocean where it is stored for decades to many centuries (Gruber et al., 2009). Due to the role of the ocean in the global carbon cycle, various ocean-based CDR methods like ocean fertilization, ocean alkalinization, restoring and increasing coastal vegetation, and marine carbon capture and storage are studied, of which Ocean Alkalinity Enhancement (OAE) shows promising results in terms of carbon storage potential and applicability (Gattuso et al., 2021). On a geological timescale, the natural drawdown of carbon by the oceans occurs through the silicate weathering process, which, however, is two orders of magnitude too slow to compensate for the current emission rates (Archer, 2005). Hence, the motivation behind OAE is to artificially accelerate the oceanic CO_2 uptake by elevating alkalinity through the dissolution of alkaline minerals like basalt, lime, olivine, calcium carbonate, or hydroxide (Caserini et al., 2022; Hartmann et al., 2013; Ilyina et al., 2013).

While it is of interest to study alkalinity addition in ocean biogeochemistry models that are agnostic to the specific alkaline material added for first order estimates of efficiency (Ilyina et al., 2013; Köhler et al., 2013), some early studies also discussed (Köhler et al., 2013) or simulated (Feng et al., 2017) the dissolution kinetics of the mineral olivine ((Mg, Fe)$_2SiO_4$) despite limited experimental data. Olivine contains iron and silicic acid, thus its application in the surface ocean has a nutrient fertilization effect in addition to the alkalinity enhancement. Olivine dissolves in the sea water according to the following chemical reaction:

$$(Mg, Fe)_2SiO_4 + 4\,CO_2 + 4\,H_2O \longrightarrow 2\,(Mg, Fe)^{2+} + 4\,HCO_3^- + H_4SiO_4 \tag{1}$$
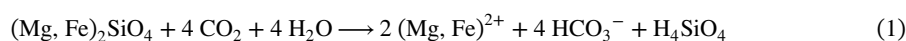
Olivine has a molar weight of 147 g mol^{-1}, and a Mg:Fe molar ratio of 9:1 is typically found in nature (De Hoog et al., 2010; Hauck et al., 2016). Accordingly, the dissolution of one mol of olivine consumes 4 mol of CO_2 and releases 4 mol of bicarbonate (HCO_3^-; alkalinity), 1 mol of silicic acid (H_4SiO_4) and 0.2 mol of iron (Equation 1). The bicarbonate effect reduces sea surface partial pressure of CO_2 (pCO_2), and thus leads to an excess flux of CO_2 from the atmosphere into the ocean (Kheshgi, 1995). The addition of iron and silicic acid during olivine dissolution leads to nutrient fertilization that stimulates phytoplankton productivity and further enhances carbon uptake. The relative contribution to CO_2 uptake by iron is 37% and silicic acid is 6%–8% (Hauck et al., 2016; Köhler et al., 2013). Iron is a limiting micronutrient for phytoplankton growth, especially in the High Nutrient Low Chlorophyll (HNLC) areas, like the Southern Ocean, equatorial Pacific, and subpolar North Pacific (De Baar et al., 1995; Smetacek et al., 2012). Hence, iron fertilization on its own is considered a marine CDR method (Aumont & Bopp, 2006; Raven & Falkowski, 1999; Zeebe & Archer, 2005).

Previous modeling studies assess OAE through various alkalinity sources, carrying out simulations using models of varying complexity at a global and regional scale (Burt et al., 2021; Hauck et al., 2016; Ilyina et al., 2013; Köhler, 2020; Lenton et al., 2018). The CDR efficiency from alkalinity enhancement was found to scale with the amount of alkaline material added, whereas nutrient effects from alkaline materials will saturate once nutrients reach levels that do not limit phytoplankton productivity anymore (Hauck et al., 2016; Köhler et al., 2013). Carbon storage through OAE has a durability of several tens to hundreds or thousand years (Köhler, 2020; Middelburg et al., 2020). The ocean CO_2 uptake per unit of alkalinity added increases with increasing atmospheric CO_2 concentration, owing to the reduced buffer capacity in a high CO_2-world (Hauck et al., 2016; Keller et al., 2014) and maximum efficiency is achieved during peak CO_2 emissions (Köhler, 2020). Although often referred to as a remedy against ocean acidification, the increase in pH remains small (0.06) by the end of the 21st century in a high-emissions scenario, for OAE done with uniform deposition of 10 Pg Ca(OH)$_2$ per year (Keller et al., 2014). This is because the initial increase in pH is compensated by the increase in CO_2 uptake after equilibration with the atmosphere (Hauck et al., 2016; Hinrichs et al., 2023). Only when a substantial reduction in atmospheric CO_2 is obtained by OAE (only measurable in model simulations when conducted in emission-driven mode), further ocean acidification is reduced (González & Ilyina, 2016; Köhler, 2020). The pH increase correlates with atmospheric CO_2 reduction across a range of CDR methods (Keller et al., 2014).

Comparing OAE in large latitudinal bands versus a global application under low and high emission scenarios revealed that OAE efficiency has limited regional sensitivity (Lenton et al., 2018). Further, climate targets are

easier to reach when OAE is applied in a low emission scneario, that is, accompanied by strong emission reduction (Lenton et al., 2018). In contrast, Burt et al. (2021) carried out OAE in large scale hydrodynamic biomes and found that regional OAE application has the potential for higher carbon uptake and OAE efficiency than global OAE. In particular, the Southern Ocean exhibited the highest CO_2 uptake efficiency, while the North Atlantic showed the lowest efficiency (Burt et al., 2021). Until now, the regional simulations of OAE were primarily focused on large tropical, subtropical or coastal depositions. Recently, some local OAE studies were also conducted, for example, for the Bering Sea (Wang et al., 2023) or the Mediterranean Sea (Butenschön et al., 2021). Other studies suggested that for a pulsed alkalinity addition, areas with long surface water residence time have the highest efficiency and deep water formation regions have a low efficiency due to the loss of alkalinity to the deep ocean (Bach et al., 2023; He & Tyka, 2023). However, an in-depth analysis of the efficacy of OAE in the deep and bottom water formation regions in the Southern Ocean and North Atlantic where carbon is transferred to abyssal ocean depths and sequestered for centennial timescale is so far missing.

Deep and bottom water formation regions are pivotal for oceanic anthropogenic carbon uptake, acting as the critical conduit for transferring carbon from the surface layer to the ocean's interior, which is the bottle-neck for ocean anthropogenic carbon uptake (Gruber et al., 2019). In general, the magnitude of anthropogenic carbon taken up by these subducting water masses depend on the rate of subduction as well as the water mass characteristics in terms of salinity and temperature (Gruber et al., 2009; Sabine et al., 2004; Walin, 1982). In the North Atlantic, the formation and downward spreading of Labrador Sea Water and North Atlantic Deep Water (NADW) result in the deepest penetration of anthropogenic carbon that reaches abyssal depths and contained ~7 PgC associated with NADW in 1994 (Sabine et al., 2004). The Antarctic Intermediate Water (AAIW) formed between 45 and 55°S contained 20 PgC in the year 1994 as a result of high wind speeds, which enhance the gas exchange, even though this water mass had very low initial anthropogenic CO_2 content due to upwelling of old waters in the vicinity (Khatiwala et al., 2009; Sabine et al., 2004). Of the three major water masses for anthropogenic carbon uptake, Antarctic Bottom Water (AABW) carries the lowest amount of anthropogenic CO_2, according to the current understanding, mainly due to limited contact of the water mass with the surface and physical barrier for CO_2 uptake due to the presence of sea ice (Sabine et al., 2004), although uncertainties are large due to scarcity of observations. However, the AABW formation region is where the carbon taken up is locked away from the atmosphere for the longest time period. Hence, overall, these subduction regions play a crucial role in oceanic anthropogenic carbon uptake and sequestration.

Recent studies suggest that subduction regions may not be optimal for OAE due to the short time for air-sea CO_2 equilibration before alkalinity is lost to the deep ocean (Bach et al., 2023; He & Tyka, 2023; Jones et al., 2014). However, our understanding of the efficiency of these regions to transfer the additional carbon taken up through OAE to the deeper ocean depths remains incomplete. In this study, we quantify the effectiveness of the deep and bottom water formation regions in the Southern Ocean, Northwest Atlantic (collective term for subduction regions in the Labrador Sea, Irminger Sea, Iceland Sea and shelf regions of Davis Strait), and the Norwegian-Barents Sea region in response to OAE in the 21st century under low and high emission scenarios. In addition to the effect of alkalinity addition, which is agnostic to the specific alkaline material added, we also diagnose the effect of nutrient fertilization that would go along with addition of the mineral olivine.

2. Methods

2.1. Model Description

We use the global ocean general circulation model FESOM2.1 (Danilov et al., 2017; Koldunov et al., 2019; Scholz et al., 2022) coupled to the ocean biogeochemistry model Regulated Ecosystem Model version 3 (REcoM3; Gürses et al., 2023). REcoM3 has 28 prognostic tracers in its standard set-up and simulates the marine carbonate system and air-sea CO_2 exchange using the mocsy routines (Orr & Epitalon, 2015). It comprises two phytoplankton classes (silicifying diatoms and small phytoplankton with an implicit representation of calcifiers), three zooplankton groups (microzooplankton, mesozooplankton, polar macrozooplankton; Karakuş et al., 2021) and resolves the cycling of the macronutrients dissolved inorganic nitrogen (DIN) and silicic acid (DSi) and the trace metal dissolved iron (DFe). The variable stoichiometry of REcoM3, that is, variable C:N:Chl:Si for diatoms and C:N:Chl:CaCO$_3$ for small phytoplankton, can, to some extent, represent the physiological response of phytoplankton to changing environmental conditions (light, nutrient availability; Schartau et al., 2007).

2.2. Experimental Setup

For this study, we use the so-called CORE mesh with 126,858 surface nodes. It has a resolution of ∼20 km along the Antarctic coast, in the equatorial region and north of 50°N, and a coarser resolution of ∼75 km in the regions with less dynamical variability, for example, in the subtropical ocean basins. In the vertical, it has 47 unevenly spaced z-levels, where layer thickness varies from 5 m at the surface to 250 m in the deep ocean. The timestep used for the simulations is 15 minutes.

As in Gürses et al. (2023), a 189 years long pre-spinup was conducted using a preindustrial atmospheric mixing ratio (xCO_2) of 278 ppm until the air-sea CO_2 flux reached a quasi-equilibrium state. The spinup used for our model simulations is the continuation of this pre-spinup with increasing atmospheric CO_2 and is conducted from 1800 to 1949. These spin-up simulations are forced by the repeating annual cycle of the year 1961 of atmospheric climate data from the JRA-55 reanalysis (Tsujino et al., 2018). Surface alkalinity restoring is switched off in the spin-up simulations and model experiments, in contrast to Gürses et al. (2023).

Following the spin-up, we perform simulations using FESOM2.1-REcoM3 from 1950 to 2100. At the ocean surface, we force the historical and future scenario simulations with the output from the AWI Climate Model (AWI-CM), precisely from its contribution to the "Coupled Model Intercomparison Project Phase 6 (CMIP6)" (Semmler et al., 2020). As in Nissen et al. (2022), the model simulations are forced with 3-hourly atmospheric momentum fluxes, freshwater fluxes, radiation and daily output of terrestrial freshwater runoff from the first ensemble member of the historical simulation until 2014 and of the SSP1-2.6 or SSP3-7.0 from 2015 until 2100 (Semmler et al., 2020).

We use the atmospheric xCO_2 from Meinshausen et al. (2017) in the historical simulation from 1950 to 2014, and the atmospheric xCO_2 from O'Neill et al. (2016) in the future projections from 2015 to 2100 under the SSP1-2.6 (low-emission) and SSP3-7.0 (high-emission) scenarios. The SSP1-2.6 scenario assumes a gradual reduction in emissions throughout the 21st century, leading to an atmospheric xCO_2 mixing ratio of 445.6 ppm by the end of the century. This scenario aligns with efforts to limit global warming to well below 2°C above preindustrial levels, and already includes some CDR. In contrast, the SSP3-7.0 scenario assumes a continuous increase in emissions, resulting in an atmospheric CO_2 mixing ratio of 867.2 ppm by the end of the 21st century. This scenario reflects inadequate climate policies and corresponds to a projected global warming of approximately 3–5°C above preindustrial levels by the end of the century (O'Neill et al., 2016).

2.3. Identifying Deep and Bottom Water Formation Regions

We use the Water Mass Transformation (WMT) framework to locate the subduction regions in the Southern Ocean (south of 40°S), Northwest Atlantic (50°N–75°N; 70°W–17°W), and the Norwegian-Barents Sea region (62°N–77°N; 60°E−10°W) using the historical simulation over the time period from 1950 to 2014. First introduced by Walin (1982), the framework enables the quantification of the magnitude at which the water in a given density class becomes denser or lighter as a result of diabatic processes such as surface fluxes, diapycnal mixing fluxes in the ocean interior, and the rate of change in the lateral transport and mixing (Abernathey et al., 2016; Nissen et al., 2022). Thus, the transformation rate represents an effective net volume flux across isopycnal surfaces, as water masses must subduct or upwell within a specified density range to ensure mass continuity when the volume flux at the ocean surface is not constant (Abernathey et al., 2016; Pellichero et al., 2018; Walin, 1982).

We relate monthly surface buoyancy fluxes, that is, heat fluxes and freshwater fluxes decomposed into contributions from evaporation minus precipitation (E-P) and sea-ice melting and formation, to the surface density distribution to derive WMT rates. As the density coordinate, we use the potential density referenced to 2,000 dbar (ρ_2; Nissen et al., 2022). Results are reported as the density anomaly, that is, $\sigma_2 = \rho_2 - 1{,}000 \text{ kg m}^{-3}$. As in Nissen et al. (2022), we divide the surface density field ρ into bins of width 0.025 kg m^{-3}. The heat flux (Q_{net}) and freshwater flux (F_{net}) transform the water masses at the atmosphere-ocean and ice-ocean interface at a WMT rate (Sv), following

$$WMT(\rho_k, t) = -\frac{1}{\rho_{k+1} - \rho_k} \iint_A \frac{\alpha Q_{net}}{\rho_0 C_p} \, dA \; + \frac{1}{\rho_{k+1} + \rho_k} \iint_A \frac{\beta S F_{net}}{\rho_0} \, dA. \qquad (2)$$

Here, A is the outcrop area between two consecutive density bins k and k + 1, ρ_0 is the reference density (35 kg m^{-3}) and S is surface salinity. The coefficients α, C$_p$ (3994 J kg^{-1} K^{-1}), and β are the thermal expansion coefficient, heat capacity, and haline contraction, respectively. The values for α, β and S were calculated as monthly means over the analysis period (1950–2014). F$_{net}$ is decomposed into freshwater fluxes between atmosphere and ocean ($F_{atm \rightarrow ocean}$, evaporation minus precipitation) and between sea ice and ocean ($F_{seaice \rightarrow ocean}$, sea-ice formation or melting):

$$F_{net} = F_{atm \rightarrow ocean} + F_{seaice \rightarrow ocean} \tag{3}$$

Water Mass Formation (WMF) rates are derived from the transformation rates in the chosen regions. The WMF rate is the derivative of the WMT rate with respect to density, and as such, a positive WMF rate represents convergence (downwelling) and a negative WMF rate denotes divergence (upwelling) in the given density bins (Abernathey et al., 2016; Pellichero et al., 2018). Following Abernathey et al. (2016) and Pellichero et al. (2018), the WMF rates are calculated by integrating over density bins of width 0.1 kg m^{-3} for the subduction regions in the Southern Ocean, Northwest Atlantic and the Norwegian-Barents Sea region.

The WMF analysis provides us with density thresholds, which facilitate the localization of the deep and bottom water formation regions in the Southern Ocean, the Northwest Atlantic and the Norwegian-Barents Sea region (Figure 2). The resulting regional olivine deposition mask is shown in Figure 2, with the individual subduction regions shown in red in the individual panels for the Southern Ocean, the Northwest Atlantic and the Norwegian-Barents Sea region. While this analysis framework identifies more regions as contributing to deep and bottom water formation than typically documented in observation-based studies (e.g., coastal regions in Davis Strait), the main formation regions and its processes are adequately captured, as discussed in more detail below.

In the Southern Ocean, subduction/downwelling occurs predominantly due to sea-ice formation in the density bins >37.0 kg m^{-3} (red-shaded regions in Figures 1a and 1b). This range of densities represent the Weddell and Ross Sea, that is, regions where the formation of Antarctic Bottom Water (AABW) takes place. The AABW formation is characterized by intense cooling and sea-ice formation resulting in dense water masses which eventually sink and spread through abyss of the global ocean (Nissen et al., 2022; Orsi et al., 1999). In the Southern Ocean between 45 and 60°S, Antarctic Intermediate and Subantarctic Mode Water (AAIW and SAMW) masses can be found, whose characteristics are set by the freshwater component of the surface buoyancy fluxes (Cerovečki & Mazloff, 2016; Hartin et al., 2011; Pellichero et al., 2018; Talley, 2008). In agreement with these studies, our model experiment suggests the E-P component of the freshwater flux lead to subduction in the density bins between 35.5 and 36.1 kg m^{-3} (Figures 1a and 1b) which represent the AAIW and SAMW formation region in the Subantarctic (Figure 2a). Buoyancy-induced upwelling in the Southern Ocean occurs between 36.1 and 37 kg m^{-3} (blue-shaded regions in Figures 1a and 1b).

In the North Atlantic, the formation of NADW mainly occurs due to heat loss (Dickson & Brown, 1994; Våge et al., 2009). The Labrador Sea Water formed as a result of deep winter-time convection in the Labrador and the Irminger Sea is entrained by the dense overflow across the Greenland-Scotland ridge and thus contributes to NADW (Jeansson et al., 2023; Våge et al., 2009). The Iceland Sea features a comparatively shallower convection leading to the formation of Iceland Intermediate Waters which also is a component of the NADW (Jeansson et al., 2017). In agreement with observation-based studies, our model also suggests heat to be the main driver for subduction in the Northwest Atlantic in the density bins <35.1 and >36.1 kg m^{-3} (Figures 1c and 1d). Heat loss also governs the subduction occurring in the Norwegian-Barents Sea region at higher densities, that is, in the density bins >36.8 kg m^{-3} (Figures 1e and 1f). Here the intermediate waters formed in the Norwegian Sea resulting from the contribution of Greenland and Iceland intermediate waters eventually contribute to the formation of NADW (Jeansson et al., 2017). Despite the fact that the Barents Sea is a comparatively shallow basin, the formation of Barents Sea Deep water and its lateral deep injection into the Nansen Basin (~1.2 km into the ocean) suggests that the Barents Sea has the potential to contribute to deep-ocean carbon storage in the Arctic (Rogge et al., 2023).

We note that the WMT framework that we use to locate the subduction regions provides only the subduction rates of the water masses in the given regions and density classes. It does not provide any explicit information on how deep a water mass can sink in the ocean, as this further depends on the vertical density structure and the entrainment of lighter water masses. Hence, depending on the model setup, the locations of these regions can
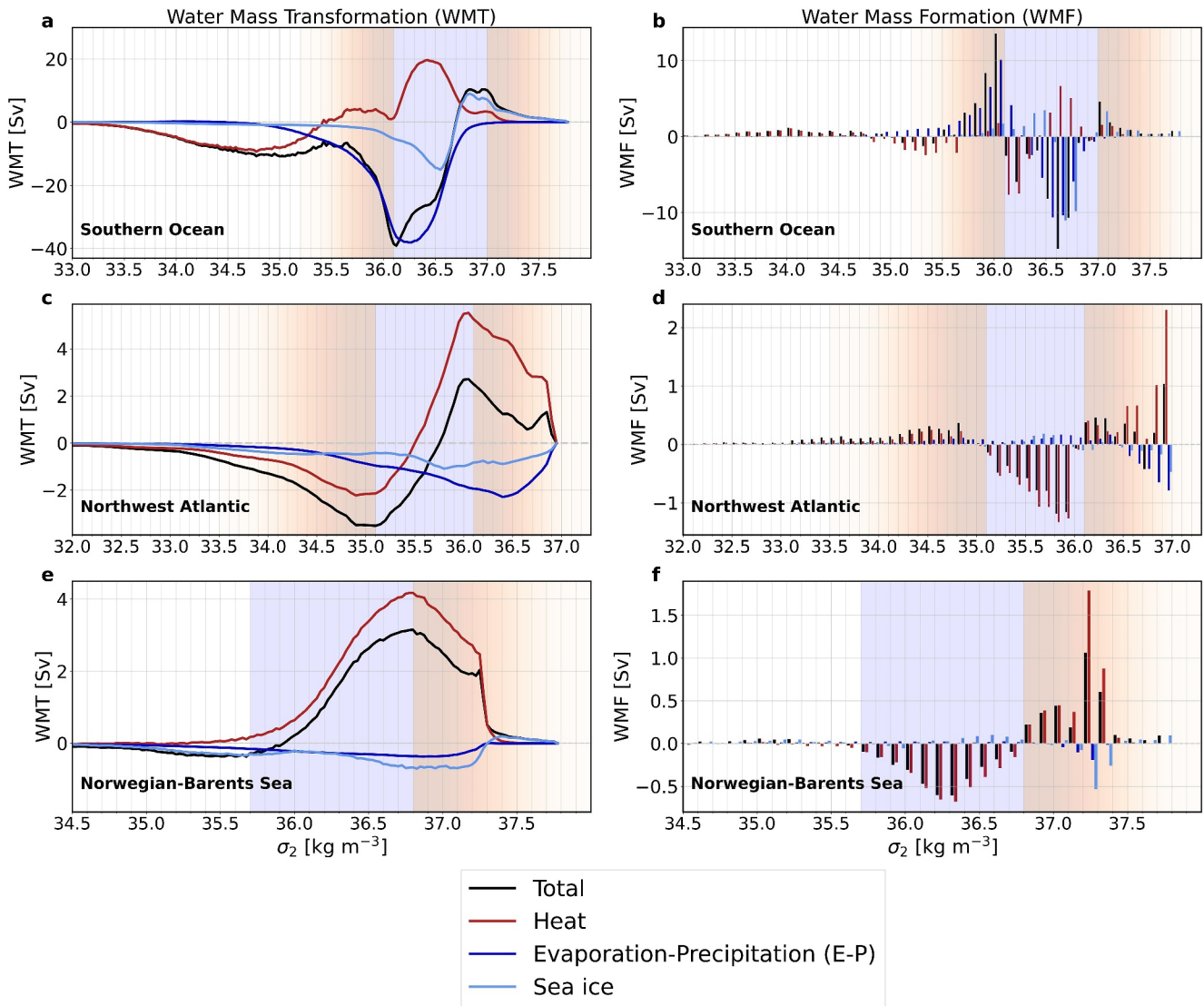
Figure 1. Water mass transformation (WMT, left) and Water mass formation (WMF, right) rates for the subduction regions. (a, c, and e) The annual mean surface WMT rates (Sv) integrated over 0.025 kg m^{-3} density bins in panel (a) the Southern Ocean, (c) the Northwest Atlantic, and (e) the Norwegian-Barents Sea region as a function of the potential density anomaly ρ_2 (kg m^{-3}) due to the total buoyancy flux (black), heat flux (red), evaporation minus precipitation (E-P; dark blue), and the sea-ice induced freshwater flux (light blue). The shading marks the density ranges of downwelling (red) and upwelling (blue). (b, d, and f) The annual mean surface WMF rates (Sv) for the different subduction regions are integrated over 0.1 kg m^{-3} density bins. The total WMF (black bars) results from the contribution of the heat flux (red bars) and the two components of the freshwater flux, that is, E-P (dark blue bars) and sea ice (light blue bars). Positive values represent subduction/downwelling (red shaded regions) and negative values represent upwelling (blue shaded regions).

differ from the real-world geographical locations of deep-water formation. In the context of OAE, we do not only consider subduction that leads to the formation of NADW in the North Atlantic and Antarctic Bottom Water in the Southern Ocean, but also the subduction that contributes to formation of subsurface water masses at intermediate depths. Despite the significant differences in physical conditions among these subduction regions (Dickson & Brown, 1994; Jeansson et al., 2017; Nissen et al., 2022; Orsi et al., 1999; Våge et al., 2009), we aggregate the results of OAE not only across all the sub-regions (Southern Ocean +Northwest Atlantic +Norwegian-Barents Sea region), but also across the sub regions with different dynamics within the Southern Ocean, Northwest Atlantic and the Norwegian-Barents Sea region. We do this to assess the collective potential for carbon uptake and storage in the Southern Ocean as well as the North Atlantic. In the remainder of the manuscript, we acknowledge that this precludes the attribution of OAE impacts to specific sub-regions. Hence, the experimental set-up
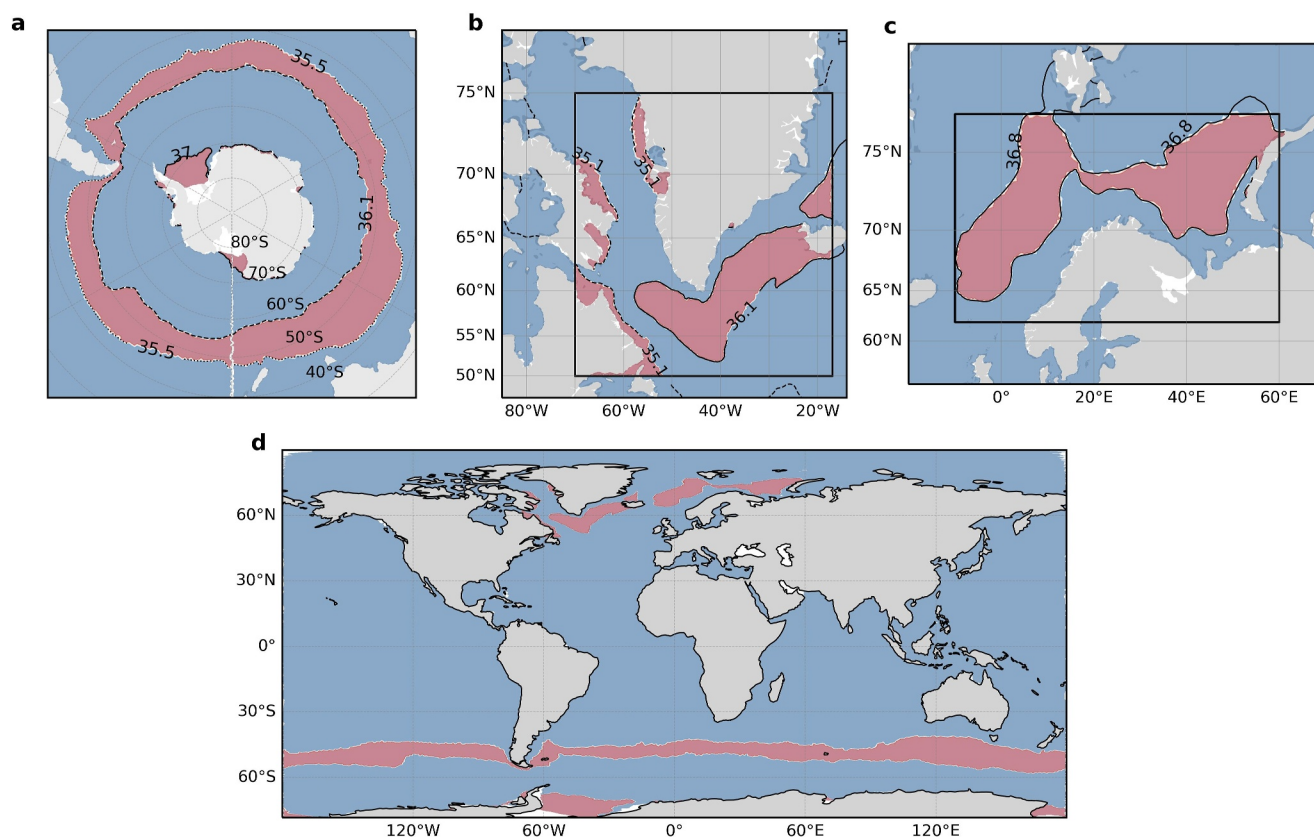
Figure 2. The regional mask for olivine deposition, obtained by using the isopycnal outcrops for deep and bottom water formation areas from the water mass formation analysis. (a) Southern Ocean. (b) Northwest Atlantic. (c) Norwegian-Barents Sea region. (d) All subduction regions combined. Red regions represent the olivine deposition areas for regional experiments (see Table 1). The black boxes for the Northwest Atlantic and the Norwegian-Barents Sea region denote the areas considered for the water mass transformation analysis. For the Southern Ocean, we consider the area south of 40°S.

described in the following section is to be understood in the context of the WMT framework applied to our model fields.

2.4. Ocean Alkalinity Enhancement Model Experiments

Following the historical simulation over 1950–2014, we conduct two simulations without olivine addition (CTRL) from 2015 to 2100 under the low-emission and the high-emission scenario. We further simulate eight OAE experiments over the period 2030–2100 under both emission scenarios, resulting in a total of 16 OAE experiments (Table 1). These experiments differ in the combinations of alkalinity and nutrient addition and region of application. We branch the OAE experiments from the scenario simulations (CTRL) in 2030 and simulate additions at a constant rate until the end of 2100. For the global simulation, we base the amount of alkalinity addition on the assumption of depositing 3 Pg yr^{-1} of olivine following (Hauck et al., 2016; Köhler et al., 2013). For all experiments, the added olivine is scaled with the modeled sea-ice cover, which is scenario dependent. As a result, the effective amount of olivine entering the ocean surface is slightly lower than 3 Pg yr^{-1} in the global case (same hold for the regional experiments, see Table 1). Thus, following Equation 1, a deposition of 2.89 Pg Olivine yr^{-1} results in 78.80 Tmol yr^{-1} alkalinity enhancement in the global experiments under the SSP3-7.0 scenario, as well as 3.94 Tmol yr^{-1} Fe^{2+} and 19.70 Tmol yr^{-1} Si input in the simulations that account for nutrient addition. Similarly, under the SSP1-2.6 emission scenario, addition of 2.86 Pg Olivine yr^{-1} results in 77.60 Tmol yr^{-1} alkalinity enhancement, 3.88 Tmol yr^{-1} Fe^{2+} and 19.40 Tmol yr^{-1} Si input. Table 1 gives the information about the amount of alkalinity and nutrients deposited for the individual subduction regions. The deposited material is assumed to be in liquid form or to be completely and instantaneously dissolved in the surface ocean. For the regional application, the same amount per area as in the global deposition is applied (8.2 g m^{-2} yr^{-1} olivine; before scaling with sea-ice cover, which leads to 0.21 mol m^{-2} yr^{-1} alkalinity), resulting in a lower total

Table 1
Overview of Model Experiments to Assess Ocean Alkalinity Enhancement for the Period 2030–2100

Experiments	Olivine deposited (Pg yr^{-1})	Effective olivine (Pg yr^{-1})		Alkalinity (Tmol yr^{-1})		Fe^{2+}(Tmol yr^{-1})		Silicic acid (Tmol yr^{-1})		Regions
		SSP3-7.0	SSP1-2.6	SSP3-7.0	SSP1-2.6	SSP3-7.0	SSP1-2.6	SSP3-7.0	SSP1-2.6	
CTRL	–	–	–	–	–	–	–	–	–	Global
GLO-ALK	3	2.89	2.86	78.80	77.60	–	–	–	–	Global
GLO-ALK-NUT	3	2.89	2.86	78.80	77.60	3.94	3.88	19.70	19.40	Global
SUB-ALK	0.22	0.21	0.21	5.72	5.72	–	–	–	–	Subduction regions combined
SUB-ALK-NUT	0.22	0.21	0.21	5.72	5.72	0.29	0.29	1.43	1.43	Subduction regions combined
SO-ALK	0.20	0.19	0.19	5.20	5.20	–	–	–	–	Southern Ocean
SO-ALK-NUT	0.20	0.19	0.19	5.20	5.20	0.26	0.26	1.30	1.30	Southern Ocean
NWA-ALK	0.014	0.013	0.012	0.35	0.33	–	–	–	–	Northwest Atlantic
NBS-ALK	0.010	0.0099	0.0098	0.27	0.26	–	–	–	–	Norwegian-Barents Sea region

Note. All simulations are conducted for the SSP1-2.6 and SSP3-7.0 scenarios, resulting in 18 model experiments. The following regions are considered: global (GLO), subduction regions combined (SUB), Southern Ocean (SO), Northwest Atlantic (NWA) and Norwegian-Barents Sea region (NBS). While the model is agnostic to the choice of alkaline material with regards to alkalinity addition, the silicic acid and iron content is derived with the assumption of olivine addition. Region-ALK represents simulations with only alkalinity addition and Region-ALK-NUT represents simulations with alkalinity +nutrients (Fe, Si) addition. Effective olivine is the amount of olivine which is deposited at the ocean surface after accounting for the modeled sea-ice cover.

deposition of alkalinity and nutrients (Table 1). Applying it to regions in which high-density water masses are subducted based on an assessment of surface buoyancy fluxes (Section 2.3), this results in a regional alkalinity addition of 5.20 Tmol yr^{-1} (SSP3-7.0 and SSP1-2.6) in the Southern Ocean (Figure 2a), 0.35 Tmol yr^{-1} (SSP3-7.0) and 0.33 Tmol yr^{-1} (SSP1-2.6) in the Northwest Atlantic (Figure 2b), and 0.27 Tmol yr^{-1} (SSP3-7.0) and 0.26 Tmol yr^{-1} (SSP1-2.6) in the Norwegian-Barents Sea region (Figure 2c). We carry out the simulations for the subduction regions individually and combined, in order to differentiate between the efficiency and contribution to carbon uptake of each region independently. When the regions are combined together, the resulting mask (Figure 2d) deposits 5.72 Tmol yr^{-1} alkalinity uniformly.

We perform OAE experiments with alkalinity addition but without nutrient addition for all five regions, globally: GLO, combined subduction regions: SUB, Southern Ocean: SO, Northwest Atlantic: NWA, Norwegian-Barents Sea region: NBS. In addition, we conduct simulations with combined alkalinity and nutrient addition for the global ocean, the area combining all subduction regions and the subduction region in the Southern Ocean. As ∼97% of the nutrient fertilization effect in the experiment combining all subduction regions occurs in the SO, we refrain from simulating the impact of nutrient addition separately for the NWA and NBS regions.

2.5. Computation of OAE Efficiency Metrics

As a first metric of efficiency, we use the excess air-sea CO$_2$ flux divided by the amount of alkaline material applied after scaling it with the sea-ice cover. This efficiency metric is referred to as CDR potential and has the unit PgC per Pg olivine (Hauck et al., 2016; Köhler et al., 2013). This metric may be considered as a short-term efficiency as it is calculated based on air-sea CO$_2$ flux in the considered period. It is calculated as the difference in the air-sea CO$_2$ flux between the OAE and the CTRL simulation (ΔCO$_2$ flux), which is then divided by the effective amount of olivine added to the surface ocean that is, accounting for the percentage of the simulated ice-free area at each time-step (15 minutes) in the calculation. We calculate the CDR potential from globally integrated values for the effect of alkalinity addition as well as the combined effect of alkalinity and nutrient addition.

As a second metric, we use the ratio of volume-integrated changes in ocean dissolved inorganic carbon (DIC) to volume-integrated alkalinity (Burt et al., 2021; Renforth & Henderson, 2017). This metric is known as ηCO$_2$ (ΔDIC/ΔAlk, unitless) and is agnostic to the alkaline material used and mode of application of OAE. It is thus highly comparable between different studies of OAE. The volume-integrated ΔDIC and ΔAlk quantify the total accumulation of DIC and alkalinity since the beginning of the alkalinity enhancement, and ηCO$_2$ can thus be

considered as a long-term efficiency metric. Specifically, ηCO_2 is computed as the difference in volume-integrated DIC between the OAE and the CTRL simulations divided by the difference in volume-integrated alkalinity between the OAE and the CTRL simulations. Thus, the effect of sea ice on alkalinity addition is accounted for. This metric (ηCO_2) targets carbonate chemistry specifics, hence, it cannot be applied to quantify the nutrient effect. As for the CDR potential, we calculate ηCO_2 from globally integrated values.

3. Results

3.1. CO₂ Flux and OAE Efficiencies

Without perturbing the oceans (CTRL), the oceanic CO_2 uptake reaches 4.52 and 0.34 PgC yr^{-1} over the last decade of the century in the SSP3-7.0 and SSP1-2.6 scenarios, respectively. OAE results in additional carbon uptake under both emission scenarios, and air-sea CO_2 flux scales to first order with the amount of alkalinity added. In general, the excess CO_2 uptake is higher in SSP3-7.0 than in SSP1-2.6, when only alkalinity addition is simulated globally and in the subduction regions (Figures 3a and 3b). For example, the global CO_2 uptake (GLO-ALK) increases by 0.9 PgC yr^{-1} for SSP3-7.0 and by 0.8 PgC yr^{-1} for SSP1-2.6 (Table 2). The SUB-ALK and SO-ALK experiments that cover 7.5% and 6.6% of the global surface ocean area, exhibit very similar excess CO_2 uptake of 0.05–0.07 PgC yr^{-1} (SSP3-7.0) and 0.05–0.06 PgC yr^{-1} (SSP1-2.6). The NWA-ALK and NBS-ALK that cover only 0.45% and 0.33% of global surface ocean area have the lowest excess CO_2 uptake (~0.003 PgC yr^{-1}). In the simulations with nutrient addition, biological productivity is enhanced, thus leading to a higher carbon uptake than in the 'only alkalinity' simulations. The global simulations (GLO-ALK-NUT) under both emission scenarios have equal increase in the CO_2 uptake (1.24 PgC yr^{-1}) which is a factor of 1.4 higher than in GLO-ALK. The excess CO_2 uptake in SUB-ALK-NUT and SO-ALK-NUT again are comparable in magnitude. Interestingly, the sensitivity to emission scenarios is reversed for the nutrient effect, as the excess CO_2 uptake is marginally higher in the SSP1-2.6 than in the SSP3-7.0 scenario (Figures 3a and 3b).

The CDR potential, defined as the excess air-sea CO_2 flux per unit of olivine deposited in the sea surface after scaling with the sea-ice cover (ΔCO_2 flux (PgC) per Pg olivine; Köhler et al. (2013)) differs substantially between the simulations with only alkalinity and with alkalinity +nutrient addition (Figures 3c and 3d). Simulating only alkalinity addition, globally or in the subduction regions, the CDR potential is marginally higher in SSP3-7.0 than in SSP1-2.6, as expected from the higher CO_2 uptake. Regional differences in the CDR potential are small with the CDR potential ranging from 0.23 to 0.27 PgC per Pg olivine for SSP1-2.6 and from 0.29 to 0.31 PgC per Pg olivine for SSP3-7.0 for the global oceans and the subduction regions (Figures 3c and 3d, Table 2).

With the addition of nutrients, the CDR potential in SSP1-2.6 is slightly higher than in SSP3-7.0 in the subduction regions (SUB-ALK-NUT and SO-ALK-NUT), while no sensitivity to emission scenario is discernible in the global application case (Figures 3c and 3d; Table 2). The nutrient effect differs strongly between regions. As expected, the SO-ALK-NUT has the highest CDR potential of 1.06 PgC per Pg olivine for SSP1-2.6 and 1.00 PgC per Pg olivine for SSP3-7.0, that is ~2.3–2.5 times that of their respective global simulations (Figure 3d and Table 2). This is predominantly due to the iron fertilization occurring in the Southern Ocean between 40°–50°S, where 73% of the total CDR potential can be explained by the nutrient effect. In contrast, for GLO-ALK-NUT, alkalinity accounts for 61% and nutrient fertilization for 39% of the total CDR potential.

As with the CDR potential, ηCO_2 (long-term efficiency $\Delta DIC/\Delta Alk$) is higher under the SSP3-7.0 than SSP1-2.6 scenario for the global and the subduction regions experiments (Table 2). The GLO-ALK, SUB-ALK, SO-ALK and NWA-ALK experiments exhibit indistinguishable ηCO_2 values of 0.84–0.85 (SSP3-7.0) and 0.79–0.80 (SSP1-2.6). Of the subduction regions, the lowest ηCO_2 levels (0.65–0.75) occur in the Norwegian-Barents Sea region (NBS-ALK) (Figures 3e and 3f). Thus, both efficiency metrics point to an insensitivity of OAE to deployment region, with the exception of ηCO_2 in the Norwegian-Barents Sea region.

Substantial differences are observed between the spatial patterns of CO_2 flux increase for OAE experiments with and without nutrient addition relative to the CTRL simulations (Figure 4). The excess CO_2 flux is confined to the regions of alkalinity addition, with a nearly uniform distribution throughout the OAE deployment areas (Figures 4a and 4b). In the simulations with nutrient addition, the Southern Ocean exhibits the highest increase in carbon uptake due to elevated iron fertilization (Figures 4c and 4d; Hauck et al. (2016)). However, while higher carbon uptake in GLO-ALK-NUT is observed nearly everywhere south of 40°S, enhanced CO_2 uptake in SUB-
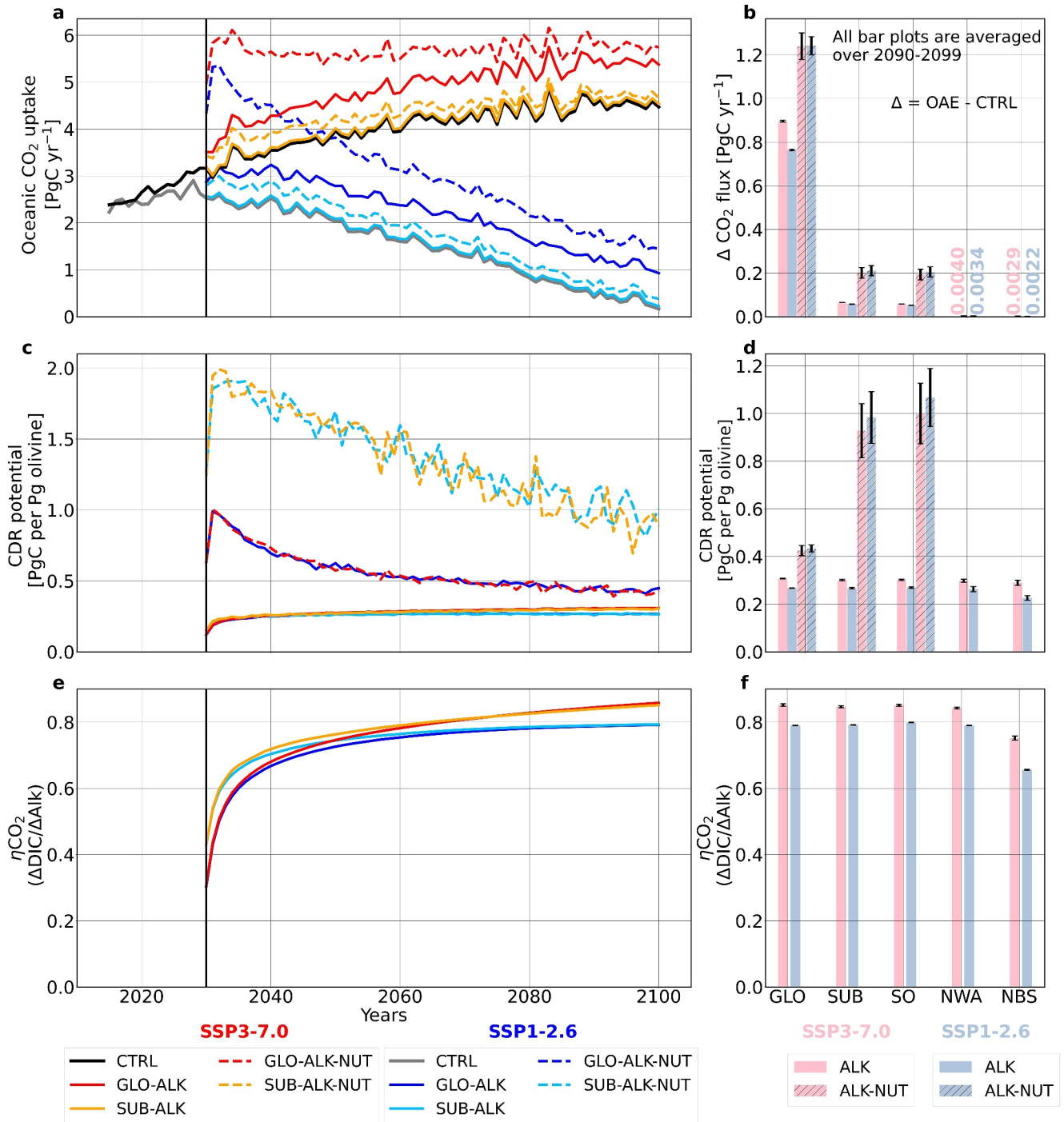
Figure 3. Response of ocean CO_2 uptake to ocean alkalinity enhancement (OAE) (Left column) Timeseries for (a) Oceanic CO_2 uptake (PgC yr^{-1}), positive values indicate a flux into the ocean, (c) Short term Carbon Dioxide Removal (CDR) potential (PgC CO_2 flux per Pg olivine) and (e) Long term OAE efficiency (ηCO_2 (unitless; $\Delta DIC/\Delta Alk$ integrated over the entire water column), under SSP1-2.6 (blue colors) and SSP3-7.0 (red colors). OAE experiments with only alkalinity addition are shown by solid lines and the experiments with alkalinity and nutrient addition by dashed lines. (Right column) Bar plots representing the average over 2090–2099 of (b) ΔCO_2 flux, (d) CDR potential and (f) ηCO_2 under SSP1-2.6 (light blue bars) and SSP3-7.0 (pink bars). Solid bars show simulations with only alkalinity addition, while hatched bars denote combined alkalinity and nutrient addition. Error bars show the standard deviation over the 2090–2099 period for the respective time series. See Table 1 for details on the model experiments.

Table 2

Excess Oceanic CO_2 Uptake (ΔCO_2 Flux), Dissolved Inorganic Carbon (ΔDIC) in the Top 1 km and >1 km, Surface Alkalinity (ΔAlk), Diatom and Small Phytoplankton Net Primary Production ($\Delta NPPd$ and $\Delta NPPn$) and Calcification Due To Ocean Alkalinity Enhancement With Respect to the CTRL Simulations

Experiments	ΔCO_2 flux (PgC yr^{-1})	ΔDIC (PgC) Top 1 (km)	>1 (km)	ΔDIC >1 km (%)	Surface ΔAlk (mmol m^{-3})	$\Delta NPPd$ (PgC yr^{-1})	$\Delta NPPn$ (PgC yr^{-1})	$\Delta Calc$ (PgC yr^{-1})	CDR pot (PgC per Pg olivine)	ηCO_2 ΔDIC ΔAlk
SSP3-7.0										
GLO-ALK	0.9	50.95	1.73	3.3	35.62	–	–	–	0.31	0.85
SUB-ALK	0.07	3.70	0.25	6.3	3.75	–	–	–	0.30	0.85
SO-ALK	0.05	3.40	0.15	4.2	3.76	–	–	–	0.30	0.85
NWA-ALK	0.004	0.20	0.06	23.1	3.25	–	–	–	0.30	0.84
NBS-ALK	0.003	0.12	0.05	29.4	2.41	–	–	–	0.29	0.75
GLO-ALK-NUT	1.24	69.51	32.43	31.8	26.84	3.53	5.91	0.13	0.43	–
SUB-ALK-NUT	0.20	11.10	7.12	39.0	4.94	0.70	0.44	0.01	0.93	–
SO-ALK-NUT	0.19	10.74	7.00	39.5	5.06	0.68	0.44	0.01	1.00	–
SSP1-2.6										
GLO-ALK	0.8	46.54	2.11	4.3	33.28	–	–	–	0.27	0.79
SUB-ALK	0.06	3.41	0.30	8.1	3.62	–	–	–	0.27	0.79
SO-ALK	0.05	3.15	0.20	5.9	3.67	–	–	–	0.27	0.80
NWA-ALK	0.003	0.17	0.06	26.1	2.91	–	–	–	0.26	0.79
NBS-ALK	0.002	0.10	0.05	33.3	2.09	–	–	–	0.23	0.65
GLO-ALK-NUT	1.24	67.31	33.90	33.5	24.70	4.32	6.60	0.15	0.43	–
SUB-ALK-NUT	0.21	11.10	7.44	40.1	4.85	0.67	0.36	0.01	0.98	–
SO-ALK-NUT	0.20	10.82	7.31	40.3	5.02	0.66	0.37	0.01	1.06	–

Note. Short-term Carbon Dioxide Removal (CDR) potential is calculated as increase in CO_2 flux per alkaline material added (PgC per Pg olivine) and ηCO_2 is the volume-integrated excess DIC over volume-integrated excess alkalinity (see Section 2.5). Efficiency metrics are calculated over the global ocean and all numbers are averaged over 2090–2099.

ALK-NUT is confined to the regions of alkalinity enhancement in the Southern Ocean, with some partly compensating reduction of carbon uptake between 60°-70°S.

3.2. Carbon Transferred to the Deep Ocean in the Form of Dissolved Inorganic Carbon (DIC)

To estimate the carbon storage potential of the subduction regions relative to the global ocean, we evaluate the enhancement in deep-ocean carbon inventory. Simulating OAE with or without nutrient addition substantially influences the amount of carbon transferred to the deep ocean (Figure 5). For GLO-ALK, the DIC inventory increases by 50.95 PgC in the top 1 km and by 1.73 PgC below 1 km compared to the CTRL under the SSP3-7.0 scenario (Figure 5a). Owing to the smaller surface area for alkalinity addition in SUB-ALK, the DIC storage increases by a lower amount, namely 3.70 PgC in top 1 km and by 0.25 PgC below 1 km (Figure 5b). Thus, 3.3% of the total ΔDIC storage in GLO-ALK occurs below 1 km, whereas the proportion rises to 6.3% for SUB-ALK. Hence, we conclude that the carbon transferred to the deep ocean is nearly twice as high for OAE in the subduction regions than in the global case (Figures 5a and 5b). In the Northwest Atlantic and Norwegian-Barents Sea region, ~25%–30% of the total carbon taken up reached below 1 km, thus making them the most effective regions for deep ocean carbon storage (Table 2).

In simulations with nutrient addition, carbon storage within the top 1 km rises by 26% for GLO-ALK-NUT and 66% for SUB-ALK-NUT compared to the respective experiments without nutrients. Due to the efficient downward transport of the biological carbon pump, carbon storage below the 1 km threshold increases by 94% in GLO-ALK-NUT and 96.5% in SUB-ALK-NUT (Figures 5c and 5d; Table 2). In the GLO-ALK-NUT experiment, the deepest carbon penetration to about ~5 km occurs in the Southern Ocean, primarily due to stimulation of
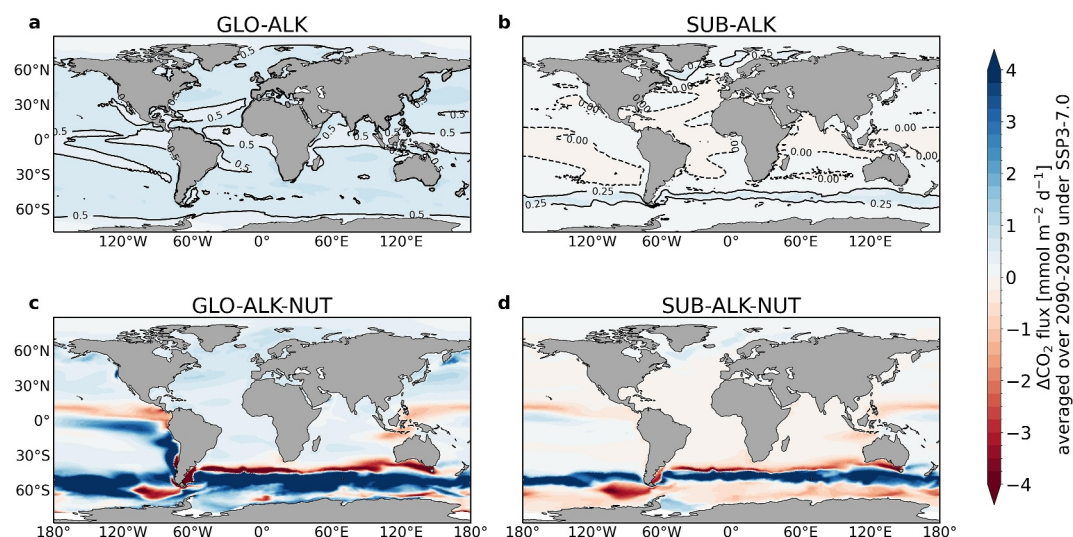
Figure 4. Spatial patterns of the difference in the CO_2 flux with respect to the CTRL run (ΔCO_2 flux), averaged over 2090–2099 for the SSP3-7.0 scenario for four experiments: (a) GLO-ALK, (b) SUB-ALK, (c) GLO-ALK-NUT, (d) SUB-ALK-NUT. Positive values (blue color) represent enhanced CO_2 uptake and negative values (red color) represent reduced CO_2 uptake compared to the CTRL simulation. See Figure S1 in Supporting Information S1 for the SSP1-2.6 scenario.

biological activity in response to nutrient fertilization (Figure 5c). Of the total increase in DIC storage relative to the CTRL, 31.8% occurs below 1 km in the GLO-ALK-NUT, while for SUB-ALK-NUT the proportion is 39%. In the SUB-ALK-NUT experiment, of the three considered subduction regions, the Southern Ocean is the dominant contributor to the carbon transfer to a depth of ∼2 km (Figure 5d). Similar conclusions can be drawn for the SSP1-2.6 scenario, where the increase in DIC storage compared to CTRL in the top 1 km has lower values globally and regionally than in the SSP3-7.0 scenario. However, more carbon is stored below 1 km (Table 2) under SSP1-2.6 than under SSP3-7.0 scenario. This can be attributed to the more stratified ocean in the higher emission scenario than in the lower emission scenario (Gattuso et al., 2015).

3.3. Net Primary Production (NPP)

Addition of nutrients leads to an increase in total Net Primary Production (NPPt) in the global and subduction region OAE experiments under both emission scenarios (Figure 6). For the GLO-ALK-NUT experiment, the increase in NPPt relative to CTRL simulation (ΔNPPt), amounts to 10.9 PgC yr^{-1} (SSP1-2.6) and 9.4 PgC yr^{-1} (SSP3-7.0) averaged over 2090–2099. As expected due to the smaller surface ocean area, the increase in NPPt for SUB-ALK-NUT is smaller, namely 1.0 and 1.1 PgC yr^{-1} in the two emission scenarios (Figure 6a). Small phytoplankton, with an implicit representation of calcification, dominate the NPPt increase with a relative contribution of 67.4% in the global experiment. In contrast, diatoms dominate the NPPt increase in the subduction region experiments with a 63.6% contribution (Figure 6b).

The spatial distribution of changes in primary productivity shows that the increase in NPPt for GLO-ALK-NUT occurs largely in the southern subtropical Pacific and the Southern Ocean (Figure 7a). The southern subtropical Pacific basin shows the largest increase in NPPn compared to other basins (Figure 7e), whereas ΔNPPd increases most in the Southern Ocean, and to a smaller extent in the equatorial Pacific, which we relate to weakened iron limitation (Figure 7c). In the SUB-ALK-NUT experiment, the increase in NPP occurs mostly in the Southern Ocean regions of alkalinity enhancement and in the equatorial upwelling region, while the subduction regions in the Northwest Atlantic and the Norwegian-Barents Sea region show no response to nutrient addition (Figure 7b). Small phytoplankton and diatom NPP exhibit similar spatial patterns, except for the signal in the equatorial Pacific basin, caused by small phytoplankton NPP (NPPn) (Figures 7d–7f).
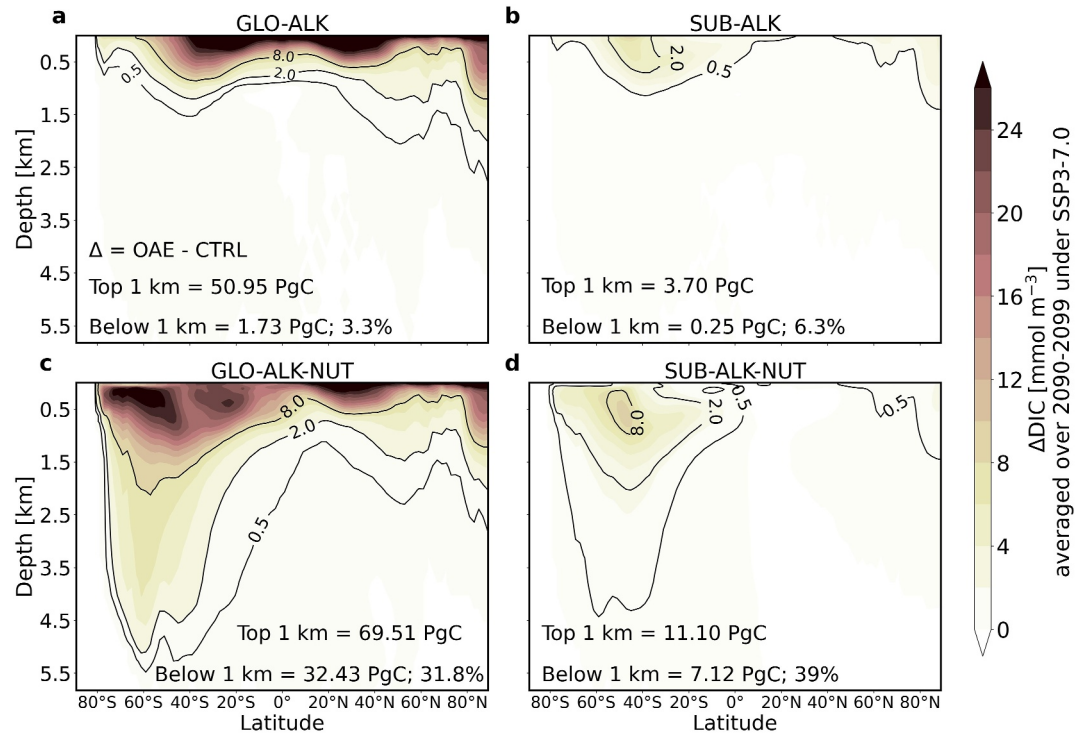
Figure 5. Zonal mean of the increase in dissolved inorganic carbon concentrations in the ocean alkalinity enhancement experiments with respect to the CTRL run (ΔDIC), averaged over 2090–2099 for SSP3-7.0 scenario for four experiments: (a) GLO-ALK, (b) SUB-ALK, (c) GLO-ALK-NUT and (d) SUB-ALK-NUT. See Figure S2 in Supporting Information S1 for the SSP1-2.6 scenario.

3.4. Surface Alkalinity and Calcification

The increase in surface alkalinity compared to the CTRL simulation scales largely with the amount of alkaline material added and thus with the areas of application, with a second-order difference between the emission scenarios. In SUB-ALK, the excess surface alkalinity per area is lower than in GLO-ALK, despite equal amounts of alkalinity being added per area. This decrease can be attributed to dilution and the loss of alkalinity to deeper ocean layers within the subduction regions (Figures 9a and 9b). Surface alkalinity also shows pronounced differences for OAE with or without nutrient addition (Figure 8). For GLO-ALK, surface alkalinity increases by
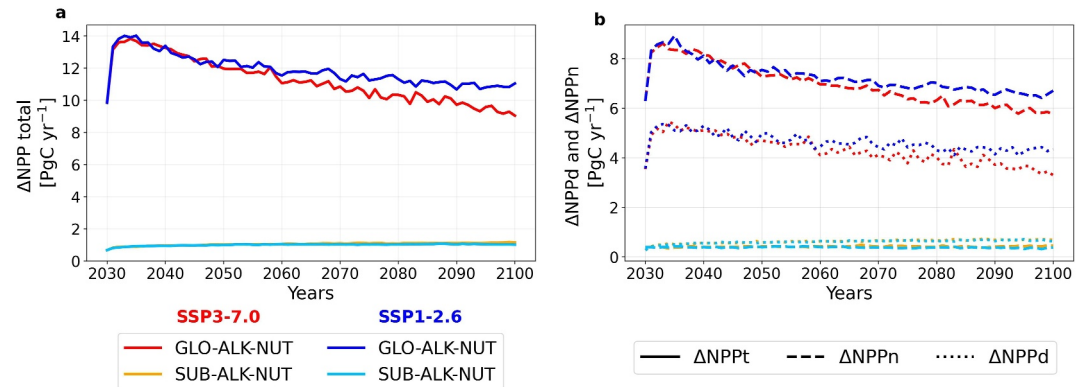

Figure 6. (a) Timeseries for excess total net primary production (NPPt) relative to the CTRL simulations (ΔNPPt; solid lines) in the ocean alkalinity enhancement experiments in PgC yr^{-1} for GLO-ALK-NUT and SUB-ALK-NUT under the SSP3-7.0 (red colors) and SSP1-2.6 (blue colors) scenarios. (b) Excess small phytoplankton NPP (ΔNPPn; dashed lines) and diatom NPP (ΔNPPd; dotted lines) for GLO-ALK-NUT and SUB-ALK-NUT.
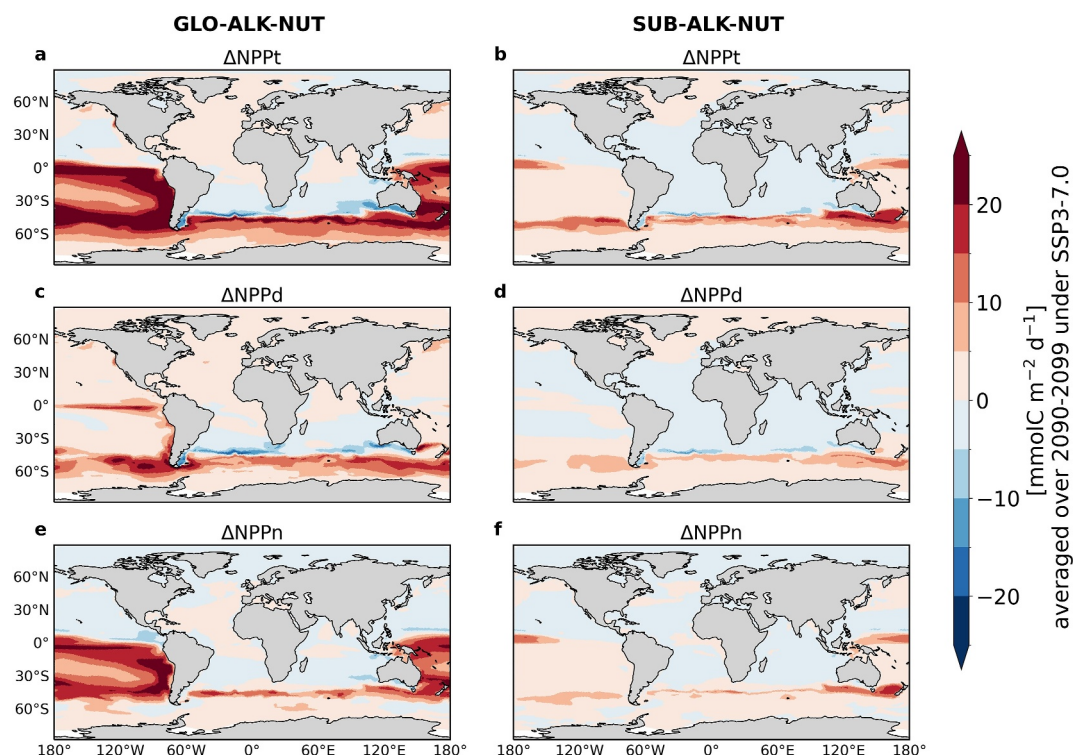
Figure 7. Spatial distribution of the excess total net primary production (ΔNPPt), diatom NPP (ΔNPPd), and small phytoplankton NPP (ΔNPPn) in the ocean alkalinity enhancement experiments relative to the CTRL simulation, averaged over 2090–2099 for the SSP3-7.0 scenario (a, c, and e) ΔNPPt, ΔNPPd, and ΔNPPn for GLO-ALK-NUT (b, d, and f) ΔNPPt, ΔNPPd, and ΔNPPn for SUB-ALK-NUT. See Figure S3 in Supporting Information S1 for the SSP1-2.6 scenario.

35.62 mmol m^{-3} (SSP3-7.0) and 33.28 mmol m^{-3} (SSP1-2.6) (Table 2). We relate these differences to distinct mixed layer and circulation between the emission scenarios. The alkalinity increase is dampened by concomitant nutrient addition and amounts to 26.84 mmol m^{-3} (SSP3-7.0) and 24.70 mmol m^{-3} (SSP1-2.6) in GLO-ALK-NUT. The 34% higher surface alkalinity in GLO-ALK than in GLO-ALK-NUT can be explained by the disproportional stimulation of small phytoplankton productivity in GLO-ALK-NUT (Figure 6b). As a result, the calcification rate is ∼23% higher in GLO-ALK-NUT than in GLO-ALK, which reduces the surface alkalinity (Figure 8; Figure 9e; Table 2).

In contrast, the excess surface alkalinity in the 2090s in the subduction region experiments is 24%–25% lower in SUB-ALK than in SUB-ALK-NUT (both emission scenarios, Figure 8; Table 2). Again, this is related to the ratio of NPPd to NPPn increase, with a stronger contribution of diatoms to the total change in NPP in the subduction region experiments (Figure 9d). This results in a positive feedback for surface alkalinity due to a higher productivity from diatoms because nitrogen assimilation of both phytoplankton groups generates alkalinity (Figure 6b). While calcification from an increase in small phytoplankton productivity would overcompensate this alkalinity generation, this is not the case for diatoms. Thus, the resulting calcification is not sufficient to reduce surface alkalinity in SUB-ALK-NUT to levels lower than in SUB-ALK, in contrast to the global experiments (Figure 9f). The Southern Ocean features a higher increase in surface alkalinity compared to other subduction regions, under both alkalinity-only and alkalinity +nutrients simulations (Table 2). As the same amount of alkalinity per surface area was added in all regions, this has to be a result of dilution by advection and mixing that is stronger in the northern hemisphere subduction regions.

3.5. Seasonality of Olivine Deposition

Ocean alkalinity enhancement leads to a response in surface alkalinity, CO_2 uptake, NPP, and DIC accumulation that varies seasonally (Figure 10). We calculate the seasonality in these parameters as the average over the regions of alkalinity addition only (Figures 2a–2c). As a consequence of alkalinity deposition being scaled with sea-ice
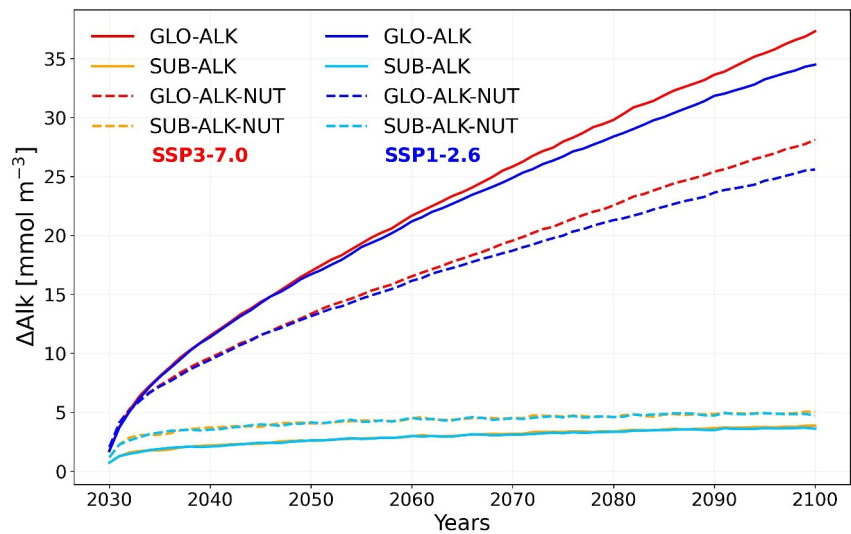
Figure 8. Timeseries of excess surface alkalinity in the ocean alkalinity enhancement experiments relative to the CTRL simulation under the SSP3-7.0 (red colors) and SSP1-2.6 (blue colors) emission scenarios. The experiments shown are GLO-ALK and SUB-ALK (solid lines), GLO-ALK-NUT and SUB-ALK-NUT (dashed lines).
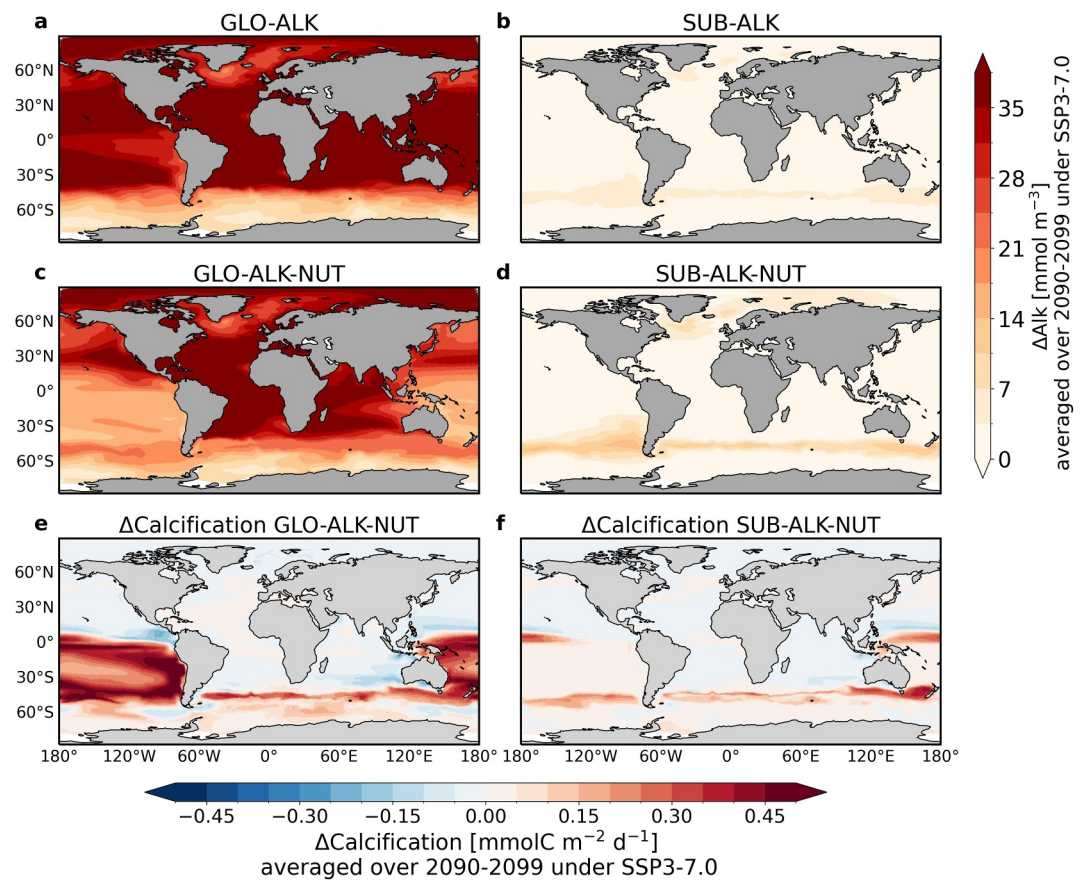

Figure 9. Spatial patterns of excess surface alkalinity and calcification in ocean alkalinity enhancement experiments relative to CTRL averaged over the years 2090–2099 under the SSP3-7.0 scenario. ΔAlk is shown for the experiments (a) GLO-ALK, (b) SUB-ALK, (c) GLO-ALK-NUT, (d) SUB-ALK-NUT and ΔCalcification for (e) GLO-ALK-NUT and (f) SUB-ALK-NUT. See Figure S4 in Supporting Information S1 for SSP1-2.6 scenario.

cover, olivine addition is at its minimum when sea-ice cover peaks in the Southern Ocean winter (July-September; Figures 10a–10c). For the Norwegian-Barents Sea region, olivine addition is almost constant throughout the year except during March-April when it is lower as the sea-ice cover increases (Figures 11a–11d). Irrespective of the seasonal variations in the alkalinity addition, the excess surface alkalinity is in phase with the seasonal changes in the Mixed Layer Depth (MLD) in both hemispheres. We quantify MLD in our model by identifying the depth at which the potential density of the water column exceeds the sea surface potential density by 0.03 kg m^{-3}. As the MLD begins to shoal in the summer months (December-April: Southern Ocean, and June-October: North Atlantic), the surface alkalinity increases more strongly relative to CTRL due to reduced mixing thus a low loss of excess alkalinity to the deep ocean (Figures 10b, 10e, and 10f; Figures 11b and 11e). In contrast, in the winter months, the deeper MLD leads to a lower ΔAlk concentration for both hemispheres (Figures 10b, 10e, and 10f; Figures 11b and 11e). As high excess surface alkalinity results in high excess CO_2 uptake, the dominant driver of CDR efficiency is MLD and its seasonal variations. We note that the simulated winter MLD in the Northwest Atlantic and specifically in the Labrador Sea is <150 m in our model, which is lower than observation-based estimates (1,000–1,550 m; Lavender et al. (2002); Lorbacher et al. (2006); Figures S7 and S8 in Supporting Information S1). This model bias is possibly due to a combination of biases in the simulated distributions of temperature and salinity in the ocean (and thus stratification) and biases in the atmospheric fields used to force our ocean-only simulations (Semmler et al., 2020). Thus, the simulated shallow MLD due to this bias in the Northwest Atlantic regions implies that our model might underestimate the excess carbon uptake and storage capacity from OAE in this region.

Evidently, the increase in the CO_2 flux relative to CTRL (ΔCO_2 flux) follows the seasonal variation of the increase in surface alkalinity (ΔAlk) and thus MLD in the Southern Ocean as well as in the North Atlantic (Figures 10b and 10e–10h; Figures 11b, 11c, and 11e). For the SO-ALK simulation, the highest ΔCO_2 flux occurs in the months of February to May with a few months lag after the MLD minimum, while the minimum is found during August to December period, again with a few months lag after the MLD maximum (Figures 10e and 10g). When including the nutrient effect (SO-ALK-NUT), ΔCO_2 flux is higher than in SO-ALK due to the excess phytoplankton production (Figure 10d). Here, the maximum additional uptake occurs during December to February and the minimum during July to September (Figure 10h). Hence, when the nutrients are included, the seasonality in excess carbon uptake relative to CTRL is shifted from April in SO-ALK to December as this is when primary production peaks in SO-ALK-NUT. In the North Atlantic, the maximum ΔCO_2 flux occurs between August and October after MLD had been at its minimum for about 3 months. The minimum ΔCO_2 flux is found between March and May for the NBS-ALK and NWA-ALK experiments (Figures 11e and 11c for Norwegian-Barents Sea region, see Figures S7 and S8 in Supporting Information S1 for the seasonality in the Northwest Atlantic).

In order to assess the seasonal cycle of excess DIC accumulation compared to the CTRL simulation (ΔDIC), we calculate the difference in ΔDIC between the consecutive months for the period December 2089 to December 2099. Afterward, the ΔDIC accumulation is averaged over the 10 year period as for the other metrics. The seasonality in ΔDIC accumulation is strongly influenced by the seasonality in the ΔCO_2 flux for the simulations in the Southern Ocean (Figures 10g–10j) and the North Atlantic (Figures 11c and 11f). The top 0.5 km layer strongly follows the variations of the ΔCO_2 flux, while the intermediate (0.5–1 km) and the bottom (>1 km) layer have only a weak seasonal cycle for all the simulations. High surface ΔDIC accumulation is observed between January and April for the Southern Ocean and between August to October in the North Atlantic regions. The deepening of the mixed layer over the winter months results in negative ΔDIC accumulation, where the CO_2 uptake happening at the surface ocean in the particular region is not sufficient to increase the DIC concentration in the water column. The lateral transport of the water masses leads to advection of DIC outside the regions of consideration, thereby reducing the DIC to levels below those in the CTRL simulation (Figures 10i and 10j; Figure 11f). For the NBS-ALK experiment, the signal below 0.5 km can be assumed to mainly stem from the Norwegian Sea as the Barents Sea is shallower than 400 m (Figure 11f), but we note that the latter has also been shown to contribute to deep-ocean carbon transfer through lateral transport (Rogge et al., 2023). In the case of SO-ALK-NUT, the negative ΔDIC accumulation is larger due to enhanced respiration and remineralization in response to the nutrient fertilization (Figure 10j).
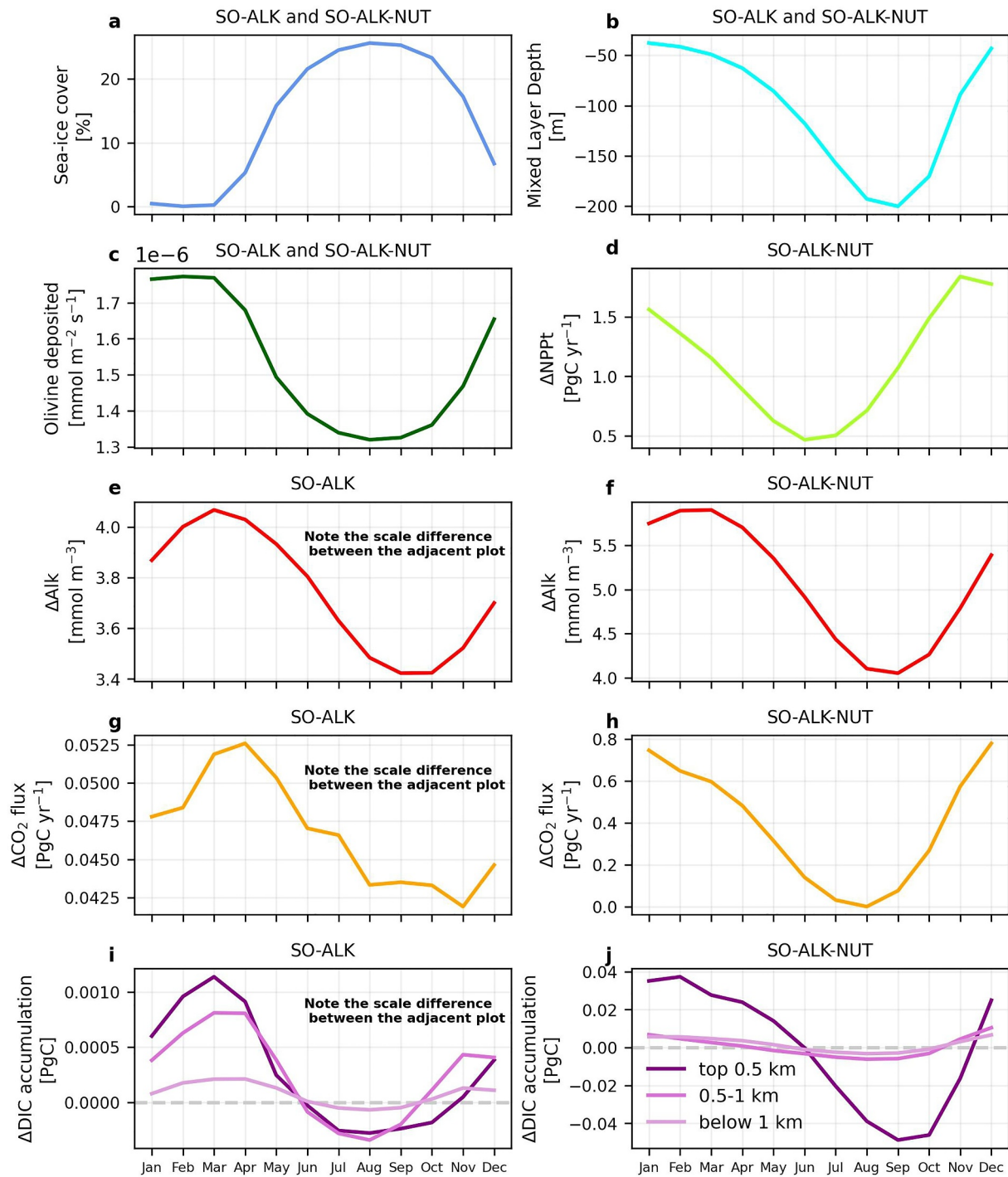
Figure 10. Seasonality for olivine deposition and biogeochemical responses in the ocean alkalinity enhancement experiments relative to CTRL in the Southern Ocean. The SO-ALK and SO-ALK-NUT simulations are shown and numbers are averaged over 2090–2099 under the SSP3-7.0 scenario. (a, b, and c) Sea-ice cover (%), Mixed Layer Depth (MLD; m) Olivine deposition (mmol m^{-2} s^{-1}) for SUB-ALK and SUB-ALK-NUT. (d) Excess Total Net Primary Production ΔNPPt (PgC yr^{-1}) for SUB-ALK-NUT (e, f) Surface ΔAlk; (mmol m^{-3}); (g, h) ΔCO$_2$ flux (PgC yr^{-1}; positive: enhanced uptake, negative: reduced uptake) and (i, j) ΔDIC accumulation (PgC; positive: increase in dissolved inorganic carbon (DIC) accumulation; negative: loss of DIC due to vertical and lateral transport) in top 0.5 km (dark purple), 0.5–1 km (orchid), below 1 km (light purple). See Figure S5 in Supporting Information S1 for a corresponding figure for the emission scenario SSP1-2.6.

4. Discussion

The aim of this study was to assess the CO_2 uptake and storage efficiency of regional OAE in the deep and bottom water formation regions in the Southern Ocean, the Northwest Atlantic and the Norwegian-Barents Sea region under both the SSP3-7.0 and SSP1-2.6 emission scenarios. In contrast to previous reports by He and Tyka (2023); Bach et al. (2023), the OAE efficiency in the subduction regions under both SSP1-2.6 and SSP3-7.0 scenarios is comparable in our model experiments to that in the global ocean when calculated based on the final decade of air-sea CO_2 fluxes (CDR potential: 0.23–0.31 PgC per Pg olivine; Table 2). When calculating the efficiency based on decades-long cumulative carbon storage (ηCO_2; depth-integrated $\Delta DIC/\Delta Alk$), only the Norwegian-Barents Sea region stands out with a lower efficiency (0.65–0.75; Table 2), whereas both the Southern Ocean and the Northwest Atlantic subduction regions still exhibit efficiencies comparable to the global ocean (0.79–0.85; Table 2). The Norwegian-Barents Sea region exhibits a lower efficiency due to its initially lower increase in DIC accumulation compared to the control simulation from 2030 to 2040. The lower ΔDIC accumulation over this period could be due to prolonged equilibration time for gas-exchange or stronger vertical transport in this basin. Either way, this lower efficiency from 2030 to 2040 ultimately affects the averaged ηCO_2 efficiency over 2090–2099 in the Norwegian-Barents Sea region.

The global OAE efficiency numbers reported in this paper are comparable to previous studies. Assessing the OAE efficiency for global OAE simulations with similar alkalinity addition as in our global simulation, Köhler et al. (2013) report an efficiency of 0.25 PgC per Pg olivine for the present-day (2000–2010). This is comparable to our global CDR potential (0.27 PgC per Pg olivine) under the SSP1-2.6 scenario (Table 2). This close agreement is rooted in the fact that the atmospheric CO_2 concentration over the period 2000–2010 is close to that in the low emission scenario SSP1-2.6. For the simulation under the SSP3-7.0 scenario, our model experiments yield a slightly higher CDR potential of 0.31 PgC per Pg of olivine. This outcome is close to the results of Hauck et al. (2016), who reported an efficiency of 0.33 PgC per Pg of olivine for a future high-emission scenario (RCP8.5) when deploying the same amount of olivine as in our simulations (Table 2). These findings confirm the small but existent scenario dependency that we will discuss below. In the context of the long-term efficiency (ηCO_2), Burt et al. (2021) reported a global efficiency of 0.79 over the last decade of their simulation under constant atmospheric CO_2 of 280 ppm when depositing 0.25 Pmol yr^{-1} of alkalinity over 75 years. This agrees well with our ηCO_2 for global OAE under the SSP1-2.6 scenario (0.79; Table 2).

The CDR potential for OAE based on air-sea CO_2 flux in the subduction regions yields values comparable to that for global OAE under both emission scenarios. This highlights that the surface efficiency of OAE is insensitive to the region of application. This agrees with Köhler et al. (2013), who found the potential for global OAE and for OAE along commercial ship tracks to be comparable. Studying broad latitudinal bands, Lenton et al. (2018) also concluded that OAE exhibits little sensitivity to the region of application. In contrast, the efficiency metric based on cumulative ΔDIC storage (ηCO_2) shows the highest efficiency in the Southern Ocean (0.85) and the lowest in the North Atlantic subduction regions, particularly the Norwegian-Barents Sea region (0.73). This agrees with Burt et al. (2021) who report a regional sensitivity of the response to OAE. The authors showcase the Southern Ocean to be the most efficient (0.89) and the subpolar North Atlantic to be the least efficient (0.7), which they attribute to the rapid loss of added alkalinity to the deep ocean.

Even though the surface CDR potential displays very low regional sensitivity in our study, the deep ocean carbon storage (below 1 km) relative to the added alkalinity in the subduction regions is nearly twice as large as compared to the global oceans (Figures 5a and 5b), acknowledging a smaller absolute magnitude in the former related to the smaller area of application (Table 2). Notably, the Northwest Atlantic and the Norwegian-Barents Sea region transfer a higher fraction (25%–30%) of the additional carbon taken up to depths below 1 km than both the global oceans and the Southern Ocean (see NWA-ALK and NBS-ALK experiments). Importantly, our results are in contrast to the findings by He and Tyka (2023); Bach et al. (2023), who suggested that deep and bottom water formation regions are not suitable for OAE due to their limited residence time at the ocean surface. While we find a reduced efficiency for the Norwegian-Barents Sea region, this cannot be confirmed for the Northwest Atlantic and the Southern Ocean. A key difference between the studies is that we simulated continuous alkalinity addition whereas He and Tyka (2023); Bach et al. (2023) assumed a pulsed deployment for a month. It remains to be tested whether the continuous addition of alkalinity may compensate for the limited residence time, thus resulting in a higher surface alkalinity and a higher OAE efficiency in the subduction regions. Siegel et al. (2021) highlighted that the carbon discharged in the deep ocean below 500 m will lead to sequestration times over decades to
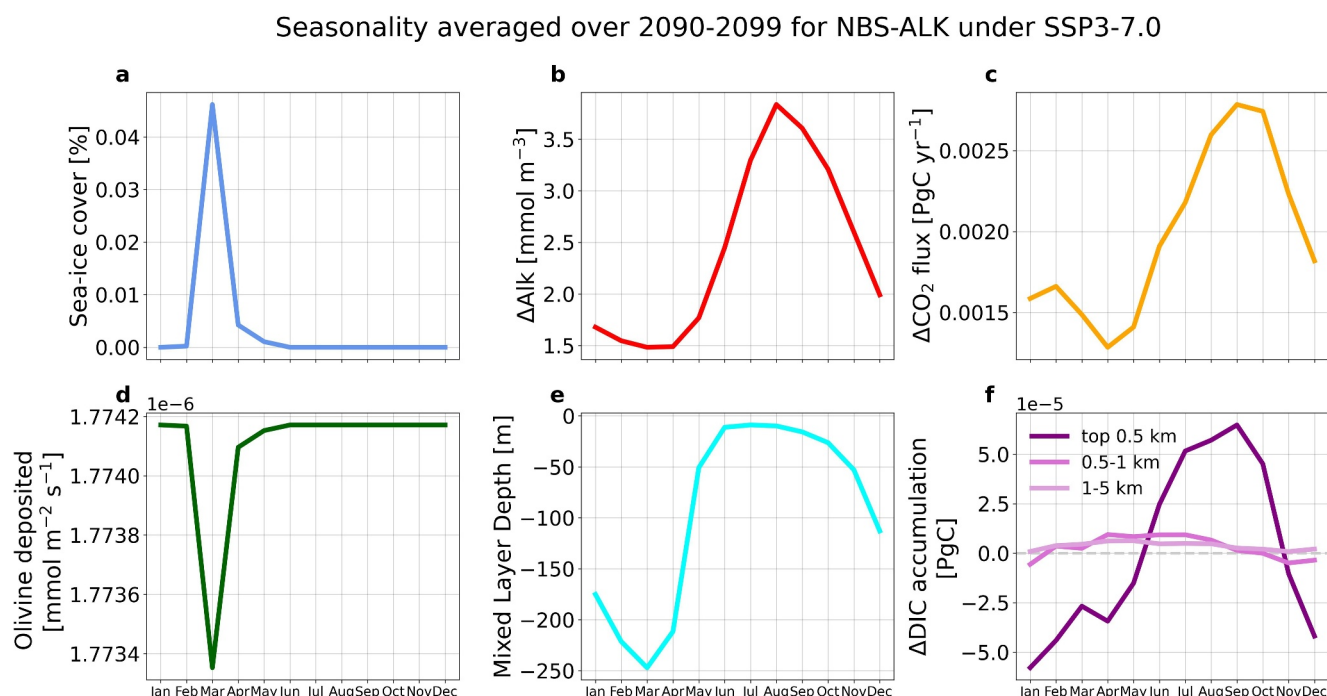
Seasonality averaged over 2090-2099 for NBS-ALK under SSP3-7.0

Figure 11. Seasonality for olivine deposition and biogeochemical responses in the ocean alkalinity enhancement experiments relative to CTRL in the Norwegian-Barents Sea region. The NBS-ALK simulation is shown and numbers are averaged over 2090–2099 under the SSP3-7.0 scenario. (a) Sea-ice cover (%), (b) Surface ΔAlk (mmol m^{-3}), (c) ΔCO_2 flux (PgC yr^{-1}; positive: enhanced uptake, negative: reduced uptake), (d) Olivine deposited (mmol m^{-2} s^{-1}) (e) Mixed Layer Depth (MLD; m), and (f) ΔDIC accumulation (PgC; positive: increase in dissolved inorganic carbon (DIC) accumulation; negative: Loss of DIC due to vertical and lateral transport) in top 0.5 km (dark purple), 0.5–1 km (orchid), below 1 km (light purple). See Figure S6 in Supporting Information S1 for the results of the NBS-ALK experiment under the SSP1-2.6 emission scenario and Figures S7 and S8 in Supporting Information S1 for the Northwest Atlantic (NWA-ALK) experiment under the SSP3-7.0 and SSP1-2.6 emission scenarios, respectively.

centuries, thus increasing the durability of OAE efficiency. This supports our hypothesis to simulate OAE in the subduction regions, which would facilitate long-term carbon storage away from the atmosphere.

The sensitivity of the CDR potential to the addition of nutrients (iron and silicic acid) along with alkalinity varies regionally. Iron availability limits primary productivity and the associated carbon uptake (Blain et al., 2007). Specifically the Southern Ocean displays a low ambient concentration of iron which acts as a limiting micro-nutrient for phytoplankton growth (Aumont & Bopp, 2006; Oschlies et al., 2010; Smetacek et al., 2012). Therefore, carrying out OAE along with nutrient addition leads to an increased drawdown of carbon through enhanced productivity. Our results thus agree with the studies by Oschlies et al. (2010); Hauck et al. (2016) which also highlight that the Southern Ocean is the most efficient region in terms of carbon uptake efficiency due to nutrient fertilization with silicic acid and iron. The CDR potential for global olivine deposition including the nutrient effects was previously reported to be 0.57 PgC per Pg olivine using the same biogeochemical model as ours but with a different physical ocean model (Hauck et al., 2016). This is slightly higher than our global CDR potential (0.43 PgC per Pg olivine; Table 2). This difference in CDR potential between our study and that of Hauck et al. (2016) can be traced back to the differing ratios of small phytoplankton to diatom productivity. In their study, the ratio stands at 0.65 compared to our 1.53, due to a higher increase in diatom productivity on their end. This led to a heightened NPP of 17.8 PgC yr^{-1} in their study, as opposed to our 10.92 PgC yr^{-1}. This distinction likely stems from difference in the background state of the simulated ecosystem.

The scenario dependency of both metrics is generally weak, but the OAE efficiencies with only alkalinity addition are slightly higher in the high-emission scenario. While the absolute CO_2 flux is higher under SSP3-7.0 due to the higher atmospheric CO_2 concentration, any additional CO_2 flux following OAE is more closely linked to the state of ocean carbonate chemistry than background CO_2 concentrations. Thus, the lower buffer capacity under SSP3-7.0 leads to a higher additional carbon uptake and in turn higher OAE efficiencies than under SSP1-2.6 (Figures 3a and 3b; Gattuso et al. (2015); Keller et al. (2014); Hauck et al. (2016)). Using an

Earth System Model, Lenton et al. (2018) reported that the low emission scenario is more efficient in terms of atmospheric CO_2 drawdown than the high emission scenario. This apparent contradiction with our results can be understood by considering their different definition of 'efficiency'. Defining OAE efficiency as the amount of OAE needed to achieve a given atmospheric temperature and CO_2 concentration target, it is unsurprising that a lower emission scenario is more effective than a high emission scenario in Lenton et al. (2018). Yet, we note that using their definition, the absolute reduction in atmospheric CO_2 concentration for a fixed OAE is comparable in Lenton et al. (2018) for both scenarios, reconciling their results with ours. In our results, we also find a scenario dependence of the fraction of carbon stored below 1 km. Under the SSP3-7.0 scenario, a lower fraction of total carbon taken up is stored below 1 km than under the SSP1-2.6 scenario (Table 2). This is due to a stronger stratification in the higher-emission scenario and thus a less efficient carbon transfer to the deeper oceans. This holds true for simulations with and without nutrient addition in the global and the subduction regions (Table 2).

The results presented here assume the complete and instantaneous dissolution of olivine as in Köhler et al. (2013); Hauck et al. (2016). Thus, our results give a theoretical upper limit of the OAE potential for global and subduction regions. However, in reality, the dissolution of olivine and in turn the OAE efficiency are influenced by the grain size, MLD and sea surface temperature (SST) (Köhler et al., 2013). Fine grain sizes of ~1 μm lead to a high residence time in the mixed layer, resulting in high OAE efficiency, whereas the efficiency decreases substantially as the grain size increases and most of the material is lost to the deep ocean undissolved (Feng et al., 2017; Köhler et al., 2013). But, the necessity of grinding the material to a very fine size is expensive in terms of energy consumption which offsets the OAE efficiency by about 30% and also poses a practical challenge in terms of mining and transportation (Caserini et al., 2022; Köhler et al., 2013; Renforth et al., 2013). One of the risks of using olivine for OAE is that, it is accompanied by addition of heavy trace metals, for example, nickel which can negatively impact the ecosystem (Hartmann et al., 2013). For instance, nickel addition leads to significant reduction in the growth rate of some phytoplanktons, for example, diatom (Guo et al., 2022; Xin et al., 2023). Thus, it is critical to assess the choice of alkaline material used for OAE considering the side effects it may have on the marine ecosystem. Similarly, sinking particulate olivine grains may have undesired effects on the benthic ecosystem through optical and mechanical stress (Feng et al., 2017). If alkalinity is excessively enhanced above a certain threshold, increased secondary $CaCO_3$ precipitation is possible (Hartmann et al., 2013; Middelburg et al., 2020). Increased $CaCO_3$ precipitation will counteract the purpose of OAE by consuming the added alkalinity and thus dampening the carbon uptake efficiency. Therefore, to avoid secondary $CaCO_3$ precipitation, it is necessary to examine the safe limits for alkalinity enhancement (Hartmann et al., 2013). Laboratory experiments for OAE using CaO and $Ca(OH)_2$ in the natural sea water collected 200–300 m offshore at New South Wales Australia were conducted by Moras et al. (2022). They found that increment of 500 μmol kg^{-1} of total alkalinity drastically reduced OAE efficiency due to increased $CaCO_3$ precipitation, while for an increase of 250 μmol kg^{-1} no $CaCO_3$ precipitation was observed, implying it to be a safe limit for OAE (Moras et al., 2022). In our simulations with uniform addition of only alkalinity, the excess surface alkalinity in SUB-ALK (3.75 mmol m^{-3}) is much smaller than in GLO-ALK (35.62 mmol m^{-3}) at comparable efficiency. This lower excess surface alkalinity in the SUB-ALK simulation is due to dilution of added alkalinity resulting from the lateral and vertical spreading, which in turn may also reduce the risk of secondary precipitation.

The temperature dependence of alkalinity addition through olivine deposition highlight that the favourable regions for maximum dissolution are between 40°N and 40°S. Additionally, the deep water formation regions in the North Atlantic, characterised by deep MLD, allow olivine to remain at the ocean surface longer, facilitating maximum dissolution. As a result, these areas are also deemed favorable for OAE (Köhler et al., 2013). However, our results suggest that the shallow MLD in summer for both hemispheres is favourable for higher OAE efficiency when dissolved alkaline material is added. This is because the added alkalinity is not lost to the deep oceans due to reduced mixing and thus results in higher CO_2 uptake and OAE efficiency. Hence, it is crucial to critically investigate the intricacies of the regions, acknowledging the distinct dynamics exhibited by various sub-regions encompassed within our regional masks for OAE. Furthermore, careful consideration of modes of application is essential to optimize OAE efficiency and mitigate negative impacts it can have on the marine ecosystems.

5. Conclusion

Simulating OAE in the subduction regions of the Southern Ocean, the Northwest Atlantic and the Norwegian-Barents Sea region revealed that these regions are as efficient as the global ocean for OAE, with the Norwegian-Barents Sea region showing a comparatively lower efficiency. It is crucial to note that we address the theoretical upper limit of OAE efficiencies, assuming instantaneous effects of added alkalinity on oceanic carbon uptake, which may not hold in practical scenarios. The time period required for added alkalinity to shift the equilibrium at the ocean surface is not accounted for and can thus introduce uncertainties in the OAE efficiencies. In terms of practical OAE implementation, coastal deployments are deemed more realistic owing to the current legal restrictions on open-ocean deployments. Acknowledging the logistical challenge associated with mining and transportation of the alkaline mineral used for OAE, it is more likely that OAE is in the form of pulsed alkalinity addition rather than the uniform continuous additions as simulated in our study. Seasonal variations in MLD influence the increase in surface alkalinity, which in turn affects carbon uptake and storage. The shallow mixed layer depths during summer are associated with higher surface alkalinity, carbon uptake and storage in both hemispheres. Hence, this accentuates the importance of identifying optimal times of the year to maximize the efficiency of OAE deployment. Although not tested in this study, the choice of alkaline mineral used for OAE would also influence the efficiency and have varying ecological impacts, depending on the mineral used. In summary, this study underscores that the subduction regions can be efficient for carbon uptake and storage due to OAE, if OAE is optimized and strategic deployment scenarios are developed.

Data Availability Statement

The data set required to reproduce the findings of this study is available in Nagwekar et al. (2024b). The Fortran source code of FESOM2.1-REcoM3 can be obtained via github (https://github.com/tanvinagwekar/fesom2/tree/OAE_Experiments) or via Zenodo (Nagwekar et al., 2024a). Analysis was performed using the open-source software Python.

References

Abernathey, R. P., Cerovecki, I., Holland, P. R., Newsom, E., Mazloff, M., & Talley, L. D. (2016). Water-mass transformation by sea ice in the upper branch of the Southern Ocean overturning. *Nature Geoscience*, *9*(8), 596–601. https://doi.org/10.1038/ngeo2749

Archer, D. (2005). Fate of fossil fuel CO_2 in geologic time. *Journal of Geophysical Research*, *110*(C9). https://doi.org/10.1029/2004JC002625

Aumont, O., & Bopp, L. (2006). Globalizing results from ocean in situ iron fertilization studies: Globalizing iron fertilization. *Global Biogeochemical Cycles*, *20*(2). https://doi.org/10.1029/2005GB002591

Bach, L. T., Ho, D. T., Boyd, P. W., & Tyka, M. D. (2023). Toward a consensus framework to evaluate air-sea CO_2 equilibration for marine CO_2 removal. *Limnology and Oceanography Letters*, *8*(5), 685–691. https://doi.org/10.1002/lol2.10330

Blain, S., Quéguiner, B., Armand, L., Belviso, S., Bombled, B., Bopp, L., et al. (2007). Effect of natural iron fertilization on carbon sequestration in the Southern Ocean. *Nature*, *446*(7139), 1070–1074. https://doi.org/10.1038/nature05700

Burt, D. J., Fröb, F., & Ilyina, T. (2021). The sensitivity of the marine carbonate system to regional Ocean Alkalinity enhancement. *Frontiers in Climate*, *3*. https://doi.org/10.3389/fclim.2021.624075

Butenschön, M., Lovato, T., Masina, S., Caserini, S., & Grosso, M. (2021). Alkalinization scenarios in the Mediterranean Sea for efficient removal of atmospheric CO_2 and the mitigation of Ocean Acidification. *Frontiers in Climate*, *3*. https://doi.org/10.3389/fclim.2021.614537

Caserini, S., Storni, N., & Grosso, M. (2022). The availability of limestone and other raw materials for Ocean Alkalinity enhancement. *Global Biogeochemical Cycles*, *36*(5). https://doi.org/10.1029/2021GB007246

Cerovečki, I., & Mazloff, M. R. (2016). The spatiotemporal structure of diabatic processes governing the evolution of subantarctic mode water in the Southern Ocean. *Journal of Physical Oceanography*, *46*(2), 683–710. https://doi.org/10.1175/JPO-D-14-0243.1

Danilov, S., Sidorenko, D., Wang, Q., & Jung, T. (2017). The finite-volumE sea ice–ocean model (FESOM2). *Geoscientific Model Development*, *10*(2), 765–789. https://doi.org/10.5194/gmd-10-765-2017

De Baar, H. J., de Jong, J. T., Bakker, D. C., Löscher, B. M., Veth, C., Bathmann, U., & Smetacek, V. (1995). Importance of iron for plankton blooms and carbon dioxide drawdown in the Southern Ocean. *Nature*, *373*(6513), 412–415. https://doi.org/10.1038/373412a0

De Hoog, J. C., Gall, L., & Cornell, D. H. (2010). Trace-element geochemistry of mantle olivine and application to mantle petrogenesis and geothermobarometry. *Chemical Geology*, *270*(1), 196–215. https://doi.org/10.1016/j.chemgeo.2009.11.017

Dickson, R. R., & Brown, J. (1994). The production of North Atlantic deep water: Sources, rates, and pathways. *Journal of Geophysical Research*, *99*(C6), 12319–12341. https://doi.org/10.1029/94JC00530

Feng, E. Y., Koeve, W., Keller, D. P., & Oschlies, A. (2017). Model-based assessment of the CO_2 sequestration potential of coastal ocean alkalinization. *Earth's Future*, *5*(12), 1252–1266. https://doi.org/10.1002/2017EF000659

Friedlingstein, P., Jones, M. W., O'Sullivan, M., Andrew, R. M., Bakker, D. C. E., Hauck, J., et al. (2022). Global carbon budget 2021. *Earth System Science Data*, *14*(4), 1917–2005. https://doi.org/10.5194/essd-14-1917-2022

Fuss, S., Lamb, W. F., Callaghan, M. W., Hilaire, J., Creutzig, F., Amann, T., et al. (2018). Negative emissions—Part 2: Costs, potentials and side effects. *Environmental Research Letters*, *13*(6), 063002. https://doi.org/10.1088/1748-9326/aabf9f

Gattuso, J.-P., Magnan, A., Billé, R., Cheung, W. W. L., Howes, E. L., Joos, F., et al. (2015). Contrasting futures for ocean and society from different anthropogenic CO_2 emissions scenarios. *Science*, *349*(6243), aac4722. https://doi.org/10.1126/science.aac4722

Gattuso, J.-P., Williamson, P., Duarte, C. M., & Magnan, A. K. (2021). The potential for oceanocean-based climate action: Negative emissions technologies and beyond. *Frontiers in Climate*, *2*. https://doi.org/10.3389/fclim.2020.575716

González, M. F., & Ilyina, T. (2016). Impacts of artificial ocean alkalinization on the carbon cycle and climate in Earth system simulations. *Geophysical Research Letters*, *43*(12), 6493–6502. https://doi.org/10.1002/2016GL068576

Gruber, N., Clement, D., Carter, B. R., Feely, R. A., van Heuven, S., Hoppema, M., et al. (2019). The oceanic sink for anthropogenic CO_2 from 1994 to 2007. *Science*, *363*(6432), 1193–1199. https://doi.org/10.1126/science.aau5153

Gruber, N., Gloor, M., Mikaloff Fletcher, S. E., Doney, S. C., Dutkiewicz, S., Follows, M. J., et al. (2009). Oceanic sources, sinks, and transport of atmospheric CO_2. *Global Biogeochemical Cycles*, *23*(1). https://doi.org/10.1029/2008GB003349

Guo, J. A., Strzepek, R., Willis, A., Ferderer, A., & Bach, L. T. (2022). Investigating the effect of nickel concentration on phytoplankton growth to assess potential side-effects of ocean alkalinity enhancement. *Biogeosciences*, *19*(15), 3683–3697. https://doi.org/10.5194/bg-19-3683-2022

Gürses, O., Oziel, L., Karakuş, O., Sidorenko, D., Völker, C., Ye, Y., et al. (2023). Ocean biogeochemistry in the coupled ocean-sea ice-biogeochemistry model FESOM2.1-REcoM3. *Geoscientific Model Development Discussions*, 1–73. https://doi.org/10.5194/gmd-2023-2

Hartin, C. A., Fine, R. A., Sloyan, B. M., Talley, L. D., Chereskin, T. K., & Happell, J. (2011). Formation rates of Subantarctic mode water and Antarctic intermediate water within the South Pacific. *Deep Sea Research Part I: Oceanographic Research Papers*, *58*(5), 524–534. https://doi.org/10.1016/j.dsr.2011.02.010

Hartmann, J., West, A. J., Renforth, P., Köhler, P., De La Rocha, C. L., Wolf-Gladrow, D. A., et al. (2013). Enhanced chemical weathering as a geoengineering strategy to reduce atmospheric carbon dioxide, supply nutrients, and mitigate ocean acidification: Enhanced weathering. *Reviews of Geophysics*, *51*(2), 113–149. https://doi.org/10.1002/rog.20004

Hauck, J., Köhler, P., Wolf-Gladrow, D., & Völker, C. (2016). Iron fertilisation and century-scale effects of open ocean dissolution of olivine in a simulated CO_2 removal experiment. *Environmental Research Letters*, *11*(2), 024007. https://doi.org/10.1088/1748-9326/11/2/024007

He, J., & Tyka, M. D. (2023). Limits and CO_2 equilibration of near-coast alkalinity enhancement. *Biogeosciences*, *20*(1), 27–43. https://doi.org/10.5194/bg-20-27-2023

Hernández-Hernández, N., Bach, L. T., Montero, M. F., Taucher, J., Baños, I., Guan, W., et al. (2018). High CO_2 under nutrient fertilization increases primary production and biomass in subtropical phytoplankton communities: A mesocosm approach. *Frontiers in Marine Science*, *5*. https://doi.org/10.3389/fmars.2018.00213

Hinrichs, C., Köhler, P., Völker, C., & Hauck, J. (2023). Alkalinity biases in CMIP6 Earth system models and implications for simulated CO_2 drawdown via artificial alkalinity enhancement. *Biogeosciences*, *20*(18), 3717–3735. https://doi.org/10.5194/bg-20-3717-2023

Ilyina, T., Wolf-Gladrow, D., Munhoven, G., & Heinze, C. (2013). Assessing the potential of calcium-based artificial ocean alkalinization to mitigate rising atmospheric CO_2 and ocean acidification: Modeling mitigation potential of aoa. *Geophysical Research Letters*, *40*(22), 5909–5914. https://doi.org/10.1002/2013GL057981

Jeansson, E., Olsen, A., & Jutterström, S. (2017). Arctic intermediate water in the Nordic seas, 1991–2009. *Deep Sea Research Part I: Oceanographic Research Papers*, *128*, 82–97. https://doi.org/10.1016/j.dsr.2017.08.013

Jeansson, E., Tanhua, T., Olsen, A., Jr Smethie, W. M., Rajasakaren, B., Ólafsdóttir, S. R., & Ólafsson, J. (2023). Decadal changes in ventilation and anthropogenic carbon in the nordic seas. *Journal of Geophysical Research: Oceans*, *128*(3), e2022JC019318. https://doi.org/10.1029/2022JC019318

Jones, D. C., Ito, T., Takano, Y., & Hsu, W.-C. (2014). Spatial and seasonal variability of the air-sea equilibration timescale of carbon dioxide. *Global Biogeochemical Cycles*, *28*(11), 1163–1178. https://doi.org/10.1002/2014GB004813

Karakuş, O., Völker, C., Iversen, M., Hagen, W., Wolf-Gladrow, D., Fach, B., & Hauck, J. (2021). Modeling the impact of macrozooplankton on carbon export production in the Southern Ocean. *Journal of Geophysical Research: Oceans*, *126*(12). https://doi.org/10.1029/2021JC017315

Keller, D. P., Feng, E. Y., & Oschlies, A. (2014). Potential climate engineering effectiveness and side effects during a high carbon dioxide-emission scenario. *Nature Communications*, *5*(1), 3304. https://doi.org/10.1038/ncomms4304

Khatiwala, S., Primeau, F., & Hall, T. (2009). Reconstruction of the history of anthropogenic CO_2 concentrations in the ocean. *Nature*, *462*(7271), 346–349. https://doi.org/10.1038/nature08526

Kheshgi, H. S. (1995). Sequestering atmospheric carbon dioxide by increasing ocean alkalinity. *Energy*, *20*(9), 915–922. https://doi.org/10.1016/0360-5442(95)00035-F

Köhler, P. (2020). Anthropogenic CO_2 of high emission scenario compensated after 3500 Years of ocean alkalinization with an annually constant dissolution of 5 Pg of olivine. *Frontiers in Climate*, *2*, 575744. https://doi.org/10.3389/fclim.2020.575744

Köhler, P., Abrams, J. F., Völker, C., Hauck, J., & Wolf-Gladrow, D. A. (2013). Geoengineering impact of open ocean dissolution of olivine on atmospheric CO_2, surface ocean pH and marine biology. *Environmental Research Letters*, *8*(1), 014009. https://doi.org/10.1088/1748-9326/8/1/014009

Koldunov, N. V., Aizinger, V., Rakowsky, N., Scholz, P., Sidorenko, D., Danilov, S., & Jung, T. (2019). Scalability and some optimization of the finite-volumE sea ice–ocean model, version 2.0 (FESOM2). *Geoscientific Model Development*, *12*(9), 3991–4012. https://doi.org/10.5194/gmd-12-3991-2019

Lavender, K. L., Davis, R. E., & Owens, W. B. (2002). Observations of open-ocean deep convection in the Labrador Sea from subsurface floats. *Journal of Physical Oceanography*, *32*(2), 511–526. https://doi.org/10.1175/1520-0485(2002)032<0511:OOOODC>2.0.CO;2

Lenton, A., Matear, R. J., Keller, D. P., Scott, V., & Vaughan, N. E. (2018). Assessing carbon dioxide removal through global and regional ocean alkalinization under high and low emission pathways. *Earth System Dynamics*, *9*(2), 339–357. https://doi.org/10.5194/esd-9-339-2018

Lorbacher, K., Dommenget, D., Niiler, P., & Köhl, A. (2006). Ocean mixed layer depth: A subsurface proxy of ocean-atmosphere variability. *Journal of Geophysical Research*, *111*(C7). https://doi.org/10.1029/2003JC002157

Meinshausen, M., Vogel, E., Nauels, A., Lorbacher, K., Meinshausen, N., Etheridge, D. M., et al. (2017). Historical greenhouse gas concentrations for climate modelling CMIP6. *Geoscientific Model Development*, *10*(5), 2057–2116. https://doi.org/10.5194/gmd-10-2057-2017

Middelburg, J. J., Soetaert, K., & Hagens, M. (2020). Ocean alkalinity, buffering and biogeochemical processes. *Reviews of Geophysics*, *58*(3). https://doi.org/10.1029/2019RG000681

Moras, C. A., Bach, L. T., Cyronak, T., Joannes-Boyau, R., & Schulz, K. G. (2022). Ocean alkalinity enhancement – Avoiding runaway CO_2 precipitation during quick and hydrated lime dissolution. *Biogeosciences*, *19*(15), 3537–3557. https://doi.org/10.5194/bg-19-3537-2022

Nagwekar, T., Nissen, C., & Hauck, J. (2024a). FESOM2.1-REcoM3 model code for OAE. (Version expt_OAE) [Software]. *Zenodo*. https://doi.org/10.5281/zenodo.10967052

Nagwekar, T., Nissen, C., & Hauck, J. (2024b). Ocean alkalinity enhancement in deep water formation regions under low and high emission pathways. (Version v1) [Dataset]. *Zenodo*. https://doi.org/10.5281/zenodo.10056552

Nissen, C., Timmermann, R., Hoppema, M., Gürses, O., & Hauck, J. (2022). Abruptly attenuated carbon sequestration with Weddell Sea dense waters by 2100. *Nature Communications*, *13*(1), 3402. https://doi.org/10.1038/s41467-022-30671-3

O'Neill, B. C., Tebaldi, C., van Vuuren, D. P., Eyring, V., Friedlingstein, P., Hurtt, G., et al. (2016). The scenario model intercomparison project (ScenarioMIP) for CMIP6. *Geoscientific Model Development*, *9*(9), 3461–3482. https://doi.org/10.5194/gmd-9-3461-2016

Orr, J. C., & Epitalon, J.-M. (2015). Improved routines to model the ocean carbonate system: Mocsy 2.0. *Geoscientific Model Development*, *8*(3), 485–499. https://doi.org/10.5194/gmd-8-485-2015

Orsi, A., Johnson, G., & Bullister, J. (1999). Circulation, mixing, and production of Antarctic bottom water. *Progress in Oceanography*, *43*(1), 55–109. https://doi.org/10.1016/S0079-6611(99)00004-X

Oschlies, A., Koeve, W., Rickels, W., & Rehdanz, K. (2010). Side effects and accounting aspects of hypothetical large-scale Southern Ocean iron fertilization. *Biogeosciences*, *7*(12), 4017–4035. https://doi.org/10.5194/bg-7-4017-2010

Pellichero, V., Sallée, J.-B., Chapman, C. C., & Downes, S. M. (2018). The Southern Ocean meridional overturning in the sea-ice sector is driven by freshwater fluxes. *Nature Communications*, *9*(1), 1789. https://doi.org/10.1038/s41467-018-04101-2

Raven, J. A., & Falkowski, P. G. (1999). Oceanic sinks for atmospheric CO_2. *Plant, Cell and Environment*, *22*(6), 741–755. https://doi.org/10.1046/j.1365-3040.1999.00419.x

Renforth, P., & Henderson, G. (2017). Assessing ocean alkalinity for carbon sequestration: Ocean Alkalinity for C Sequestration. *Reviews of Geophysics*, *55*(3), 636–674. https://doi.org/10.1002/2016RG000533

Renforth, P., Jenkins, B., & Kruger, T. (2013). Engineering challenges of ocean liming. *Energy*, *60*, 442–452. https://doi.org/10.1016/j.energy.2013.08.006

Riahi, K., Schaeffer, R., Arango, J., Calvin, K., Guivarch, C., Hasegawa, T., et al. (2022). Mitigation pathways compatible with long-term goals. In *IPCC, 2022: Climate change 2022: Mitigation of climate change. Working group III contribution to the sixth assessment report of the intergovernmental panel on climate change* P. R. Shukla, J. Skea, R. Slade, A. Al Khourdajie, R. van Diemen, D. McCollum, M. Pathak, S. Some, P. Vyas, R. Fradera, M. Belkacemi, A. Hasija, G. Lisboa, S. Luz, & J. Malley, (Eds.), (pp. 295–408). Cambridge University Press. https://doi.org/10.1017/9781009157926.005

Rogge, A., Janout, M., Loginova, N., Trudnowska, E., Hörstmann, C., Wekerle, C., et al. (2023). Carbon dioxide sink in the Arctic Ocean from cross-shelf transport of dense Barents Sea water. *Nature Geoscience*, *16*(1), 82–88. https://doi.org/10.1038/s41561-022-01069-z

Sabine, C. L., Feely, R. A., Gruber, N., Key, R. M., Lee, K., Bullister, J. L., et al. (2004). The oceanic sink for anthropogenic CO_2. *Science*, *305*(5682), 367–371. https://doi.org/10.1126/science.1097403

Schartau, M., Engel, A., Schröter, J., Thoms, S., Völker, C., & Wolf-Gladrow, D. (2007). Modelling carbon overconsumption and the formation of extracellular particulate organic carbon. *Biogeosciences*, *4*(4), 433–454. https://doi.org/10.5194/bg-4-433-2007

Scholz, P., Sidorenko, D., Danilov, S., Wang, Q., Koldunov, N., Sein, D., & Jung, T. (2022). Assessment of the Finite-VolumE Sea ice–Ocean Model (FESOM2.0) – Part 2: Partial bottom cells, embedded sea ice and vertical mixing library CVMix. *Geoscientific Model Development*, *15*(2), 335–363. https://doi.org/10.5194/gmd-15-335-2022

Semmler, T., Danilov, S., Gierz, P., Goessling, H. F., Hegewald, J., Hinrichs, C., et al. (2020). Simulations for CMIP6 with the AWI climate model AWI-CM-1-1. *Journal of Advances in Modeling Earth Systems*, *12*(9), e2019MS002009. https://doi.org/10.1029/2019MS002009

Siegel, D. A., DeVries, T., Doney, S. C., & Bell, T. (2021). Assessing the sequestration time scales of some ocean-based carbon dioxide reduction strategies. *Environmental Research Letters*, *16*(10), 104003. https://doi.org/10.1088/1748-9326/ac0be0

Smetacek, V., Klaas, C., Strass, V. H., Assmy, P., Montresor, M., Cisewski, B., et al. (2012). Deep carbon export from a Southern Ocean iron-fertilized diatom bloom. *Nature*, *487*(7407), 313–319. https://doi.org/10.1038/nature11229

Talley, L. D. (2008). Freshwater transport estimates and the global overturning circulation: Shallow, deep and throughflow components. *Progress in Oceanography*, *78*(4), 257–303. https://doi.org/10.1016/j.pocean.2008.05.001

Tsujino, H., Urakawa, S., Nakano, H., Small, R. J., Kim, W. M., Yeager, S. G., et al. (2018). JRA-55 based surface dataset for driving ocean–sea-ice models (JRA55-do). *Ocean Modelling*, *130*, 79–139. https://doi.org/10.1016/j.ocemod.2018.07.002

UNFCCC. (2015). United nations framework on climate change (UNFCCC): Adoption of the Paris agreement, 21st conference of the parties. Retrieved from https://unfccc.int/sites/default/files/english_paris_agreement.pdf

Våge, K., Pickart, R. S., Thierry, V., Reverdin, G., Lee, C. M., Petrie, B., et al. (2009). Surprising return of deep convection to the subpolar North Atlantic Ocean in winter 2007–2008. *Nature Geoscience*, *2*(1), 67–72. https://doi.org/10.1038/ngeo382

Walin, G. (1982). On the relation between sea-surface heat flow and thermal circulation in the ocean. *Tellus*, *34*(2), 187–195. https://doi.org/10.1111/j.2153-3490.1982.tb01806.x

Wang, H., Pilcher, D. J., Kearney, K. A., Cross, J. N., Shugart, O. M., Eisaman, M. D., & Carter, B. R. (2023). Simulated impact of ocean alkalinity enhancement on atmospheric CO_2 removal in the Bering Sea. *Earth's Future*, *11*(1). https://doi.org/10.1029/2022EF002816

Xin, X., Faucher, G., & Riebesell, U. (2023). Phytoplankton response to increased nickel in the context of ocean alkalinity enhancement. *Biogeosciences Discussions*, 1–15. https://doi.org/10.5194/bg-2023-130

Zeebe, R. E., & Archer, D. (2005). Feasibility of ocean fertilization and its impact on future atmospheric CO_2 levels. *Geophysical Research Letters*, *32*(9). https://doi.org/10.1029/2005GL022449